Antarctic Ocean and Sea Ice Response to Ozone Depletion: A Two-Time-Scale Problem

DAVID FERREIRA* AND JOHN MARSHALL

*Department of Earth, Atmospheric, and Planetary Sciences, Massachusetts Institute of Technology,
Cambridge, Massachusetts*

CECILIA M. BITZ

Atmospheric Sciences Department, University of Washington, Seattle, Washington

SUSAN SOLOMON AND ALAN PLUMB

*Department of Earth, Atmospheric, and Planetary Sciences, Massachusetts Institute of Technology,
Cambridge, Massachusetts*

(Manuscript received 29 April 2014, in final form 27 October 2014)

ABSTRACT

The response of the Southern Ocean to a repeating seasonal cycle of ozone loss is studied in two coupled climate models and is found to comprise both fast and slow processes. The fast response is similar to the interannual signature of the southern annular mode (SAM) on sea surface temperature (SST), onto which the ozone hole forcing projects in the summer. It comprises enhanced northward Ekman drift, inducing negative summertime SST anomalies around Antarctica, earlier sea ice freeze-up the following winter, and northward expansion of the sea ice edge year-round. The enhanced northward Ekman drift, however, results in upwelling of warm waters from below the mixed layer in the region of seasonal sea ice. With sustained bursts of westerly winds induced by ozone hole depletion, this warming from below eventually dominates over the cooling from anomalous Ekman drift. The resulting slow time-scale response (years to decades) leads to warming of SSTs around Antarctica and ultimately a reduction in sea ice cover year-round. This two-time-scale behavior—rapid cooling followed by slow but persistent warming—is found in the two coupled models analyzed: one with an idealized geometry and the other with a complex global climate model with realistic geometry. Processes that control the time scale of the transition from cooling to warming and their uncertainties are described. Finally the implications of these results are discussed for rationalizing previous studies of the effect of the ozone hole on SST and sea ice extent.

1. Introduction

The atmospheric circulation over the Southern Ocean (SO) has changed over the past few decades, notably during austral summer, with the pattern of decadal change closely resembling the positive phase of the southern annular mode (SAM). Throughout the troposphere, pressure has trended downward south of 60°S and upward between 30° and 50°S in summer (Thompson

* Current affiliation: Department of Meteorology, University of Reading, Reading, United Kingdom.

Corresponding author address: David Ferreira, Department of Meteorology, University of Reading, P.O. Box 243, Reading RG6 6BB, United Kingdom.
E-mail: d.g.ferreira@reading.ac.uk

and Solomon 2002; Marshall 2003; Thompson et al. 2011). This pattern of pressure change is associated with a poleward shift of the westerly winds. These circulation trends have been attributed in large part to ozone depletion in the stratosphere over Antarctica (Gillett and Thompson 2003; G. J. Marshall et al. 2004; Polvani et al. 2011). During the same period, an expansion of the Southern Hemisphere sea ice cover has been observed, which most studies find to be significant (Zwally et al. 2002; Comiso and Nushio 2008; Turner et al. 2009). This expansion is observed in all seasons but is most marked in the fall (March–April–May). This is in stark contrast with the large decrease of Arctic sea ice coverage observed over recent decades (Turner et al. 2009).

The ozone-driven SAM and sea ice trends could be related. However, several published studies using coupled climate models consistently show a warming of the

SO surface and sea ice loss (in all seasons) in response to ozone depletion (Sigmond and Fyfe 2010; Bitz and Polvani 2012; Smith et al. 2012; Sigmond and Fyfe 2014). These studies concluded that the ozone hole did not contribute significantly to the expansion of the SO sea ice cover over the last three decades [see also the review by Previdi and Polvani (2014)]. This leaves us with an even bigger question: how could the SO sea ice cover increase in the face of both ozone depletion and global warming if both processes induce loss? The quandary is further complicated by the correlation between the SAM and ocean–sea ice variability found in both observations and models (Watterson 2000; Hall and Visbeck 2002; Sen Gupta and England 2006; Ciasto and Thompson 2008). Interannual variability in the SAM has a robust sea surface temperature (SST) signature: a dipole in the meridional direction with a strong zonal symmetry. For a positive phase of the SAM, SST cools around Antarctica (south of about 50°S) and warms around 40°S. This response is understood as one that is mainly forced by Ekman currents and to a lesser extent air–sea fluxes (i.e., mixed layer dynamics). A positive phase of the SAM is also associated with sea ice expansion at all longitudes except in the vicinity of Drake Passage (Lefebvre et al. 2004; Sen Gupta and England 2006; Lefebvre and Goosse 2008). Although difficult to measure, the Southern Ocean sea ice cover as a whole appears to increase slightly following a positive SAM. If this were the only important process at work, then one would expect a positive SAM-like atmospheric response to ozone depletion to drive SST cooling and sea ice expansion around Antarctica (and a SST warming around 40°S) in the long term. This scenario is reinforced by the clear resemblance between the pattern of sea ice concentration trends and the pattern of the sea ice response to a positive SAM. Following this chain of thought, Goosse et al. (2009) pointed to the ozone-driven SAM changes as the main driver of the observed SO sea ice expansion. This behavior, however, contradicts results from coupled climate models.

In this study, we attempt to reconcile the expectations from the aforementioned observed SAM–SST correlations with those from coupled modeling studies including a representation of ozone depletion. In particular, we compute the transient ocean response to a step function in ozone depletion, but one that includes the seasonal cycle of depletion, in two coupled climate models: the MITgcm and CCSM3.5. As we shall see, this exposes the elemental processes and time scales at work. The approach, in direct analogy to the climate response functions (CRFs) for greenhouse gas forcing, is described in general terms in Marshall et al. (2014). We find that the SST response to ozone depletion is made up of two phases in both models

(as summarized in the schematic in Fig. 1): a (fast) dipole response with a cooling around Antarctica (consistent with SAM–SST correlations on interannual time scales), followed by a slow warming at all latitudes south of 30°S. This warming eventually leads to a sign reversal of the SST response around Antarctica, and a switch to a positive SST response throughout the SO, consistent with previous coupled GCM experiments.

Concomitant with SST fluctuations around Antarctica, our models display increases in sea ice extent in the cooling phase followed by a decrease as SST warms. The long-term response of SST and sea ice in our models is consistent with the conclusions of previous authors. The short-term response, however, suggests that ozone depletion may have contributed to the observed sea ice expansion of the last decades (see Marshall et al. 2014). The period during which sea ice could expand in response to ozone depletion depends on the processes that control the time scale of the SST and sea ice reversal. While the reversal occurs in both models, they exhibit a rather disparate time scale of transition from warming to cooling. Reasons for these differences are discussed.

Our paper is set out as follows. In section 2, the coupled GCM setups and experimental designs are described. The ocean and sea ice responses to an abrupt ozone depletion and their mechanisms in the MITgcm and in CCSM3.5 are described in sections 3 and 4, respectively. Using a simple analytical model, in section 5 we identify key processes that account for the different time scales in the two coupled GCMs. Finally, conclusions are given in section 6.

2. Coupled model setups

a. The MITgcm

We use the MITgcm in a coupled ocean–atmosphere–sea ice simulation of a highly idealized Earthlike aquaplanet. Geometrical constraints on ocean circulation are introduced through "sticks" that extend from the top of the ocean to its flat bottom (Marshall et al. 2007; Enderton and Marshall 2009; Ferreira et al. 2010) but present a vanishingly small land surface area to the atmosphere above. In the "Double Drake" configuration employed here, two such sticks separated by 90° of longitude extend from the North Pole to 35°S, defining a small basin and a large basin in the Northern Hemisphere and a zonally reentrant Southern ocean. There is no landmass at the South Pole.

The atmospheric model resolves synoptic eddies, has a hydrological cycle with a representation of convection and clouds, a simplified radiation scheme, and an atmospheric boundary layer scheme (following Molteni 2003). The atmosphere is coupled to an ocean and

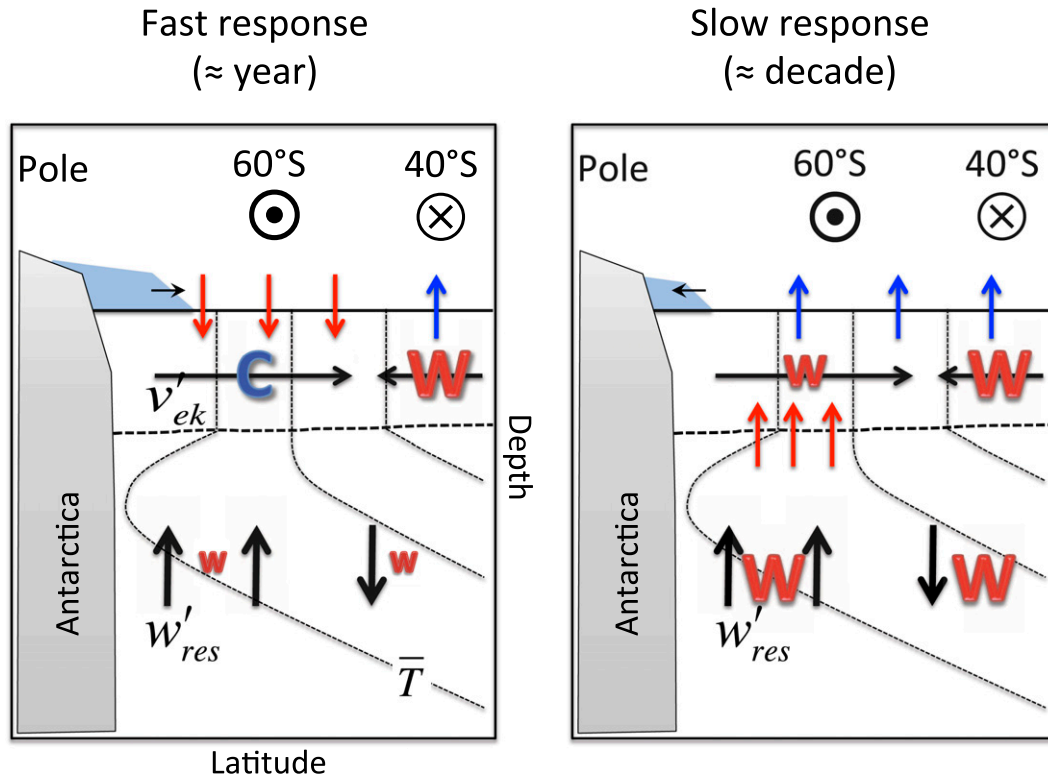## Fast response
(≈ year)

Slow response
(≈ decade)

FIG. 1. Schematic of the two-time-scale response of the ocean and sea ice to an abrupt ozone depletion, capturing the common features of the two GCMs: (left) the fast response, similar to the signature of the interannual SAM seen in observations, is dominated by the surface dynamics; and (right) the slow response, seen in coupled GCMs, is driven by the ocean interior dynamics. Black arrows denote anomalous ocean currents. Red (blue) arrows denote heat fluxes in (out) of the surface mixed layer (marked by a thick horizontal dashed line). Blue patches represent the sea ice cover (expanding in the fast response and contracting in the slow response). The thin dashed lines mimic the structure of isotherms in the Southern Ocean, showing in particular the temperature inversion found south of the ACC. Small vertical displacements (~10 m) of these isotherms (not represented in the schematic) generate temperature anomalies in the ocean interior.

a thermodynamic sea ice model [based on the formulation of Winton (2000)] driven by winds and air–sea heat and moisture fluxes. In the ocean, effects of mesoscale eddies are parameterized as an advective process (Gent and McWilliams 1990) and an isopycnal diffusion (Redi 1982) using an eddy transfer coefficient of $1200 \, m^2 \, s^{-1}$. Convection is parameterized as described in Klinger et al. (1996). The coupled model is integrated forward using the same dynamical core (Marshall et al. 1997a,b; J. Marshall et al. 2004) on the conformal cubed sphere (Adcroft et al. 2004). In calculations presented here, present-day solar forcing is employed, including a seasonal cycle, with present-day levels of greenhouse gas forcing. More details can be found in the appendix.

Despite the idealized continents, Double-Drake's climate has many similarities with today's earth (Ferreira et al. 2010). Deep water is formed in the northern part of the narrow Atlantic-like basin and is associated with a deep overturning circulation extending into the Southern Ocean where it upwells isopycnally under the combined action of surface winds and (parameterized) eddies. In contrast, the wide, Pacific-like basin is primarily wind driven. A vigorous current, analogous to the Antarctic Circumpolar Current (ACC) develops in the Southern Hemisphere in thermal wind balance with steep outcropping isopycnals. The sea ice cover is perennial poleward of 75°S, but expands seasonally to about 65°S in September (an increase of about 13.5 million km² in sea ice area), similar to today's seasonal variations in the Southern Ocean (e.g., Parkinson and Cavalieri 2012). In accord with observations, the simulated ocean stratification south of the ACC is controlled by salinity, with temperature increasing at depth (notably because of the seasonal cycle of sea ice). This temperature inversion will turn out to be a central factor controlling the rate of subsurface warming under seasonal sea ice found in response to SAM forcing.

Ozone is not explicitly computed in the model, but its shortwave absorption in the lower stratosphere is represented (the model includes a single layer representing
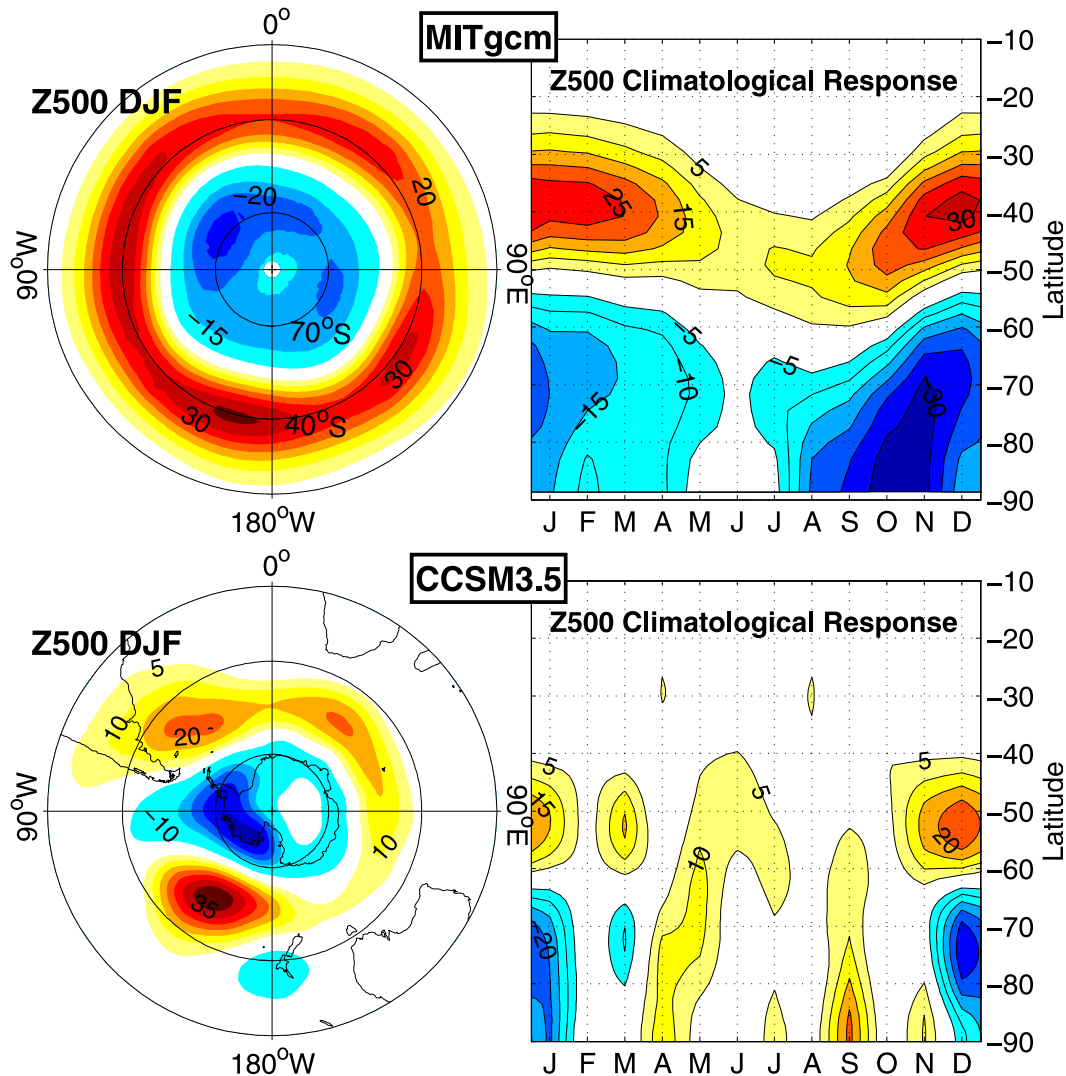
FIG. 2. Response of the geopotential height at 500 mb (m) to an abrupt ozone depletion: (left) in DJF and (right) zonal-mean climatological response for (top) the MITgcm and (bottom) CCSM3.5. The colored contour intervals are 5 m. The time average is over the first 20 yr.

the lower stratosphere). Our "ozone hole" perturbation is introduced by reducing the ozone-driven shortwave absorption south of 60°S in this layer. The imposed ozone reduction is close to 100% at the October–November boundary as observed in the lower stratosphere but is tapered down to 20% in spring (i.e., there is a minimum ozone depletion of 20% throughout the year). This perturbation is comparable to that observed in the heart of the ozone hole during the mid- to late 1990s (e.g., Solomon et al. 2007). The same perturbation is repeated every year. Note also that the ozone radiative perturbation is scaled by the incoming solar radiation and disappears during the polar night at high latitudes.

The forced response is computed as the difference between the ensemble average of the perturbed runs and the climatology of a 300-yr-long control run. Twenty 40-yr-long simulations with independent initial conditions (in both ocean and atmosphere) taken from the control run are carried out and monthly-mean outputs taken. A total of 8 of those are integrated up to 350 yr, by which point the coupled system approaches a new equilibrium.

Although our atmospheric model is simplified, it produces an atmospheric response to ozone depletion that is rather similar to that found in more complex atmospheric and coupled GCMs (e.g., Gillett and Thompson 2003; Sigmond et al. 2010; Polvani et al. 2011): pressure decreases poleward of 50°S and increases in the 50°–20°S band during the summer. This is illustrated in Fig. 2 (top) where the geopotential height at 500 mb is plotted. The geopotential response vanishes during the winter months.
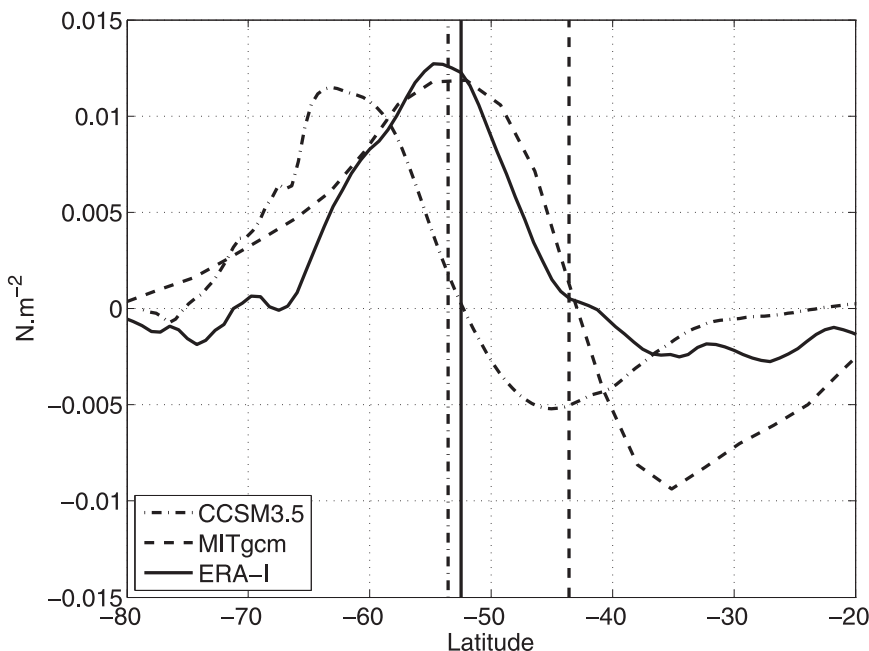
FIG. 3. Annual- and zonal-mean response of the surface wind stress ($N m^{-2}$) to an abrupt
ozone depletion in the MITgcm (dashed) and in CCSM3.5 (dashed–dotted). The time average
is over the first 20 yr. For comparison, the difference in surface wind stress between pre–ozone
hole conditions (1980–89) and peak ozone hole conditions (1995–2004) is shown from the
ERA-Interim reanalysis (solid). The vertical lines indicate the locations of the peak mean
surface wind stress.

There is an associated strengthening–weakening of the
westerly wind around 50°–30°S, as shown in Fig. 3. The
amplitude of the anomaly, ±40 m at 500 mb, is also com-
parable to those obtained in other studies in response to
a mid-1990s ozone depletion (Gillett and Thompson
2003). At the surface, the westerly wind stress anomaly is
order $0.02 N m^{-2}$ at its summer peak corresponding to
a sea level pressure response of ±3 mb, both comparable
to those found by Sigmond et al. (2010) and Polvani et al.
(2011).

Note that, as in other GCMs, the atmospheric response
to ozone depletion strongly projects onto the dominant
mode of atmospheric variability (as defined through an
EOF analysis), which resembles the observed SAM. We
do not explore the dynamics of this atmospheric response
here, but it is linked to a cooling of the lower stratosphere
and a seasonal SAM-like tropospheric anomaly. Instead,
we focus on the transient response of the ocean and sea
ice to the atmospheric anomalies. But, first, let us describe
analogous calculations carried out with the NCAR
Community Climate Model.

b. CCSM3.5

We use CCSM3.5 configured as in Gent et al. (2010),
Kirtman et al. (2012), Bitz and Polvani (2012), and Bryan
et al. (2014). All four studies describe the simulated climate

of the CCSM3.5 and the latter two focus on the Southern
Ocean and Antarctic sea ice therein. The atmospheric
component has a finite-volume dynamical core and a
horizontal resolution of 0.47° × 0.63° with 26 vertical
levels. The horizontal grid of the land is the same as the
atmosphere. The ocean and sea ice have a resolution of
nominally 1°. The ocean eddy parameterization employs
the Gent and McWilliams (GM) form (as in MITgcm),
but with a GM coefficient varying in space and time fol-
lowing Ferreira et al. (2005), as described in Danabasoglu
and Marshall (2007).

All of our integrations with CCSM3.5 have green-
house gases and aerosols fixed at 1990s level. The initial
conditions were taken from a 1990s control simulation
carried out with the CCSM3. The CCSM3.5 was first run
for 155 years (see Kirtman et al. 2012) with ozone con-
centrations intended to be representative of 1990s levels
that were prepared for the CCSM3 1990s control in-
tegrations (see Kiehl et al. 1999). However, compared to
more recent estimates of ozone concentrations from the
Atmospheric Chemistry and Climate and Stratospheric
Processes and their Role in Climate (AC&C/SPARC)
dataset (Cionni et al. 2011), the CCSM3 estimates for
the 1990s resemble the level of ozone depletion in the
Antarctic stratosphere of approximately 1980, or about
half the level of depletion since preindustrial times.

Hence, to create a quasi-equilibrated "high ozone" control integration, with preindustrial-like ozone concentrations, we ran an integration where we first ramped up the ozone concentration for the first 20 yr by adding a quantity each month equal to 1/40th of the difference between the decadal mean for the 2000s and 1960s for a given month of the AC&C/SPARC dataset. We then stabilized the ozone concentrations at this 1960s level of the AC&C/SPARC dataset for another 50 years. From the last 30 yr of this 1960s ozone level simulation, we ran an ensemble of 26 "abrupt low ozone" integrations. The prescribed ozone perturbation is equal to the seasonally varying 2000s minus 1960s difference from the AC&C/SPARC dataset. At first, six ensemble members were branched on 1 January and ran for 20 yr. At which point we realized that, to examine the very rapid response seen in the first years, a significantly larger ensemble would be required. To optimize resources, these perturbed experiments were started just before the summer season, rather than in the midst of it. Therefore, we ran another 20 ensemble members, branched on 1 September and run for 32 months. We use the six longer members to investigate behavior only beyond the first 32 months.

In total, 20 of the ensemble members, with an annual cycle as in the MITgcm, were branched on 1 September and ran for 32 months, and 6 of the ensemble members were branched on 1 January and ran for 20 yr.

As in the MITgcm, the atmospheric response to ozone depletion in CCSM3.5 is a positive SAM-like pattern with a maximum amplitude in December–January–February (Fig. 2, bottom). The pattern is similar to that found in other models (see Thompson et al. 2011) albeit with stronger zonal asymmetries, notably marked by a large trough centered on 90°W. At the peak of the summer response, geopotential height anomalies at 500 mb are about ±20 m, somewhat weaker than those seen in the MITgcm. At the surface, however, sea level pressure anomalies are typically ±3 mb and are associated with surface wind anomalies of about 1 m s^{-1} (see Bitz and Polvani 2012), similar to those in the MITgcm. Given the differences between the two coupled models, their surface responses to ozone depletion are remarkably similar although the response in CCSM3.5 has larger zonal asymmetries.

In the zonal mean, the wind stress responses of the two models are similar in shape and magnitude although they are shifted relative to one another in latitudinal direction (Fig. 3). For comparison, the surface wind stress difference between "peak ozone hole" and "pre–ozone hole" conditions, estimated from the ERA-Interim reanalysis (Dee et al. 2011), is shown in solid. The two models' responses fall on both sides of the change found in the reanalysis. Son et al. (2010) and Sigmond and Fyfe (2014)

found a relationship between the tropospheric response to ozone depletion and the location of the climatological jet in models participating, respectively, to the CCMVal-2 and CMIP5 intercomparison projects. We do not find such relationships here, except that the locations of the peak responses and those of the mean jets are arranged latitudinally in the same sequence. In particular, there is no indication that the magnitude of the response correlates with the mean jet position. Also, despite its realistic mean jet stream, the response of CCSM3.5 sits farther away from the reanalysis change than that of the MITgcm. These differences could reflect the differences in the representation of the ozone hole in the two models as well as differences in their mean states and internal dynamics linking the stratospheric cooling to the surface wind stress response. We emphasize that the correlations found by Son et al. (2010) and Sigmond and Fyfe (2014) are extracted from tens of models, but exhibit significant scatter; our small sampling here makes it difficult to draw robust conclusions.

3. Ocean and sea ice response in the MITgcm

a. The evolution of the transient SST response

Following the atmospheric response to ozone depletion, the ocean and sea ice cover adjust to the changing winds (Fig. 4). The early (years 0–5) SST response consists of a zonally symmetric dipole: a cooling between 50° and 70°S and a warming in the band 50°–25°S (there is also a weak cooling north of 25°S). This initial SST response is of significant magnitude, typically ±0.3°C, and is nearly identical to the SST signature of a positive SAM on interannual time scales seen in the MITgcm and similar to that seen in observations and other coupled GCMs (see, e.g., Watterson 2000; Hall and Visbeck 2002; Ciasto and Thompson 2008). It is primarily generated by anomalous Ekman currents (see below). After two decades or so, the SST response changes noticeably (Fig. 4, bottom left). The warm pole (50°–30°S) has nearly doubled in magnitude while the cold pole has weakened.

The ocean response is not limited to the surface (Fig. 4, right). Temperatures at 170 m exhibit a widespread warming south of 30°S with a peak around 40°S, with a slight cooling north of 30°S. The pattern of the subsurface response does not change over time but exhibits, as at the surface, a warming tendency at all latitudes south of 30°S. After two decades, the subsurface temperature peaks markedly at two latitudes, 40° and 60°S, where the anomalies reach up to 0.8°C, comparable in strength to the SST anomalies.

A continuous monitoring of the SST evolution over the first 40 years after the ozone hole inception shows that the initial dipole SST response (south of 25°S)
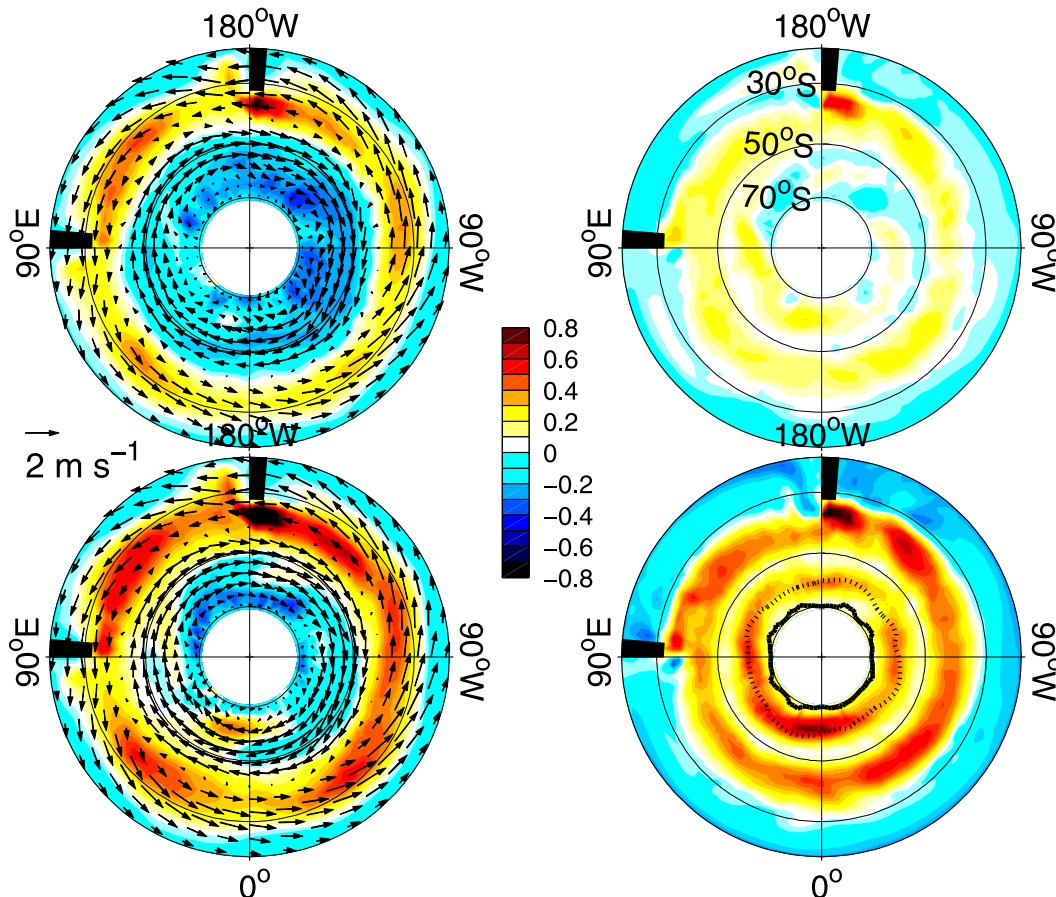
FIG. 4. Response of (left) SST (°C) and surface wind (m s^{-1}) and (right) potential temperature (°C) at 170 m averaged over years (top) 1–5 and (bottom) 16–20 after ozone hole inception in the MITgcm.

slowly morphs into a warming (Fig. 5, top). By year 40, the character of the SST response more closely mirrors the subsurface temperature pattern than the early SST response. It is notable that the long-term SST adjustment (30 yr and longer) is similar to that found by Sigmond and Fyfe (2010) and Bitz and Polvani (2012) in response to ozone depletion. These previous studies did not present or discuss the time evolution of the ocean response. Sigmond and Fyfe (2010) carried out 100-yr perturbation–control experiments and defined the response to ozone depletion as the 100-yr-averaged difference between the perturbed and control runs although they mention that the sea ice extent response in their model reaches equilibrium within 5 yr. Bitz and Polvani (2012) carried out perturbation experiments in which the ozone hole was ramped up for 20 yr and then maintained for an additional 30 yr. They defined the response to ozone depletion as the difference between perturbed and control runs averaged over the last 30 yr of integration. Clearly, in both cases, the responses were largely dominated by the long (multidecadal) adjustments of the model ocean to ozone depletion.

Our results, however, suggest that there are two phases in the SST response: a fast response, which has a dipole pattern, consistent with expectations from SAM–SST correlations on interannual time scales, followed by a slow widespread warming of the SO similar to results from previous GCMs studies. The transition between the two phases is seen after about 20 yr in the MITgcm, when the initial cold SST response in the band 50°–70°S transitions to warming. SST variations in this band are particularly important because it coincides with the region of seasonal sea ice fluctuations.

A closer look at the time evolution of the SST in the band 50°–70°S is shown in Fig. 6 (left). The area-averaged SST falls by −0.3°C within a year and then slowly and almost linearly rises to cross zero around year 20. The SST increases for 200 yr or so approaching a new equilibrium, which is 1.5°C warmer than in the control run (not shown). Ozone-depleting substances are no longer being emitted, so in the real world this forcing will not be present long enough for such a response to be realized. It is computed here to illustrate physical processes.
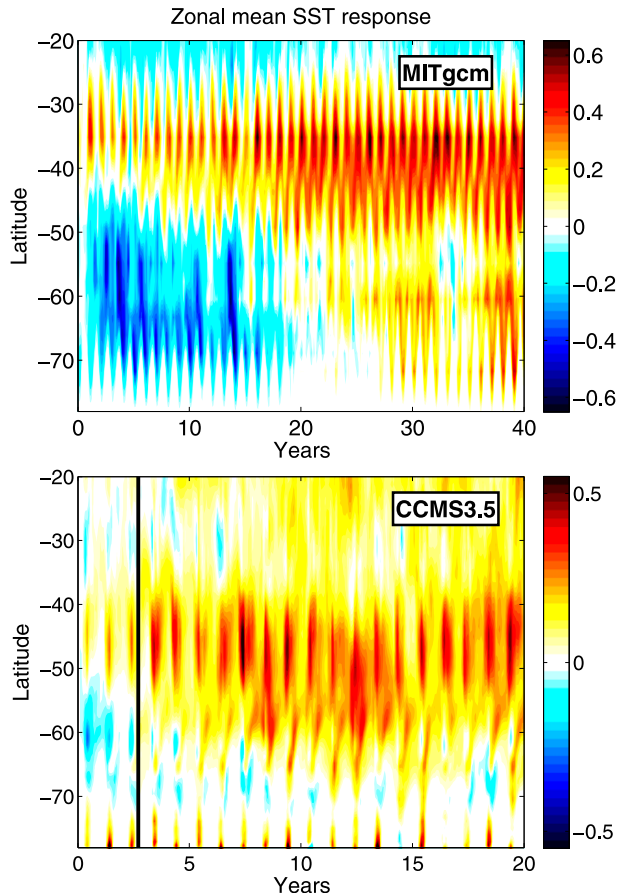
FIG. 5. Zonal-mean SST response (monthly means, °C) in (top) the MITgcm and (bottom) CCSM3.5. In the bottom panel, the vertical line separates the first 32 months when 20 ensemble members are averaged from the later months where just 6 ensemble members are averaged.

Despite the 20-member ensemble, significant noise remains in the ensemble-mean area-averaged SST due to internal variability. The gray shading and solid black line in Fig. 6 give a measure of the uncertainties in the time evolution of the SST.[1] This suggests that the fast SST response ranges between −0.1° and −0.4°C while the time of the sign reversal varies between 15 and 30 yr.

In concert with SST changes around 70°–50°S, the sea ice area also significantly evolves in response to ozone depletion (Fig. 7). As expected, sea ice expands in the presence of colder SSTs and retreats when SSTs become

---

[1] They are computed as follows: 20 × 8 realizations of the SST response are constructed by forming all possible combinations of 1 of the 20 short runs (years 0–40) with 1 of the 8 long runs (years 41–350). Each evolution is then fitted to a two-time-scale exponential form [see Eq. (8) below]. The solid black line is the mean of these 160 evolutions, while the gray shading indicates ±1 standard deviation.

positive, after about 20 yr. This increase is seen in all seasons but is largest in winter when sea ice extent is at its peak. Note that the cold SST response is largest in summer when the atmospheric perturbations are the strongest but persists throughout the year (see Fig. 5). The sea ice perturbations are small but significant, representing typically 5%–10% of the climatological seasonal change.

b. Role of interior ocean circulation in SST evolution

We now address the mechanisms that drive the evolution of the SST response.

1) THE FAST RESPONSE

On short (~year) time scales the ocean response is essentially confined to the mixed layer. The SST dipole is primarily forced by Ekman current anomalies due to the SAM-like surface wind response (Fig. 4). South of 45°S, increased surface westerly winds result in an anomalous northward Ekman flow that advects cold water from the south. North of 45°S, the opposite happens. The SST tendency due to this forcing $v' \partial_y \overline{T}$ is plotted in Fig. 8 (dashed–dotted) along with the SST response (red, both averaged over years 2–5). Here, $\partial \overline{T}/\partial y$ is taken from the control, while the full anomalous Eulerian currents v', not just its Ekman component, are used in the computation. For convenience, the tendency is expressed in watts per meter squared (W m^{-2}) taking a seawater density ρ_o of 1030 kg m^{-3}, a water heat capacity C_p of 3996 J kg^{-1} K^{-1}, and a constant mixed layer depth h_s of 30 m (the thickness of the top model level). The pattern of anomalous advection tendency closely matches that of the SST dipole and is of the correct magnitude to explain the SST response (except north of 25°S where vertical advection is an important forcing, see below).

In contrast, the net air–sea flux anomaly F' (dominated by the latent contribution, positive downward) damps the SST anomaly to the atmosphere (Fig. 8, solid black). Net air–sea heat fluxes and horizontal advection term (dashed–dotted) closely oppose one another over the first few years. The initial SST dipole is thus the quasi-equilibrium response to the fast mixed layer dynamics:

$$\frac{\partial T'}{\partial t} \simeq -v' \partial_y \overline{T} + F'_a - \lambda T' \simeq 0, \qquad (1)$$

where the net air–sea heat flux anomaly F' is made up of two contributions: a term F'_a driven by changes in the atmospheric state (independent of SST anomalies, e.g., surface wind changes, shortwave changes) and a SST damping term that varies linearly with T' on a time scale λ^{-1} (positive λ implies a damping to the atmosphere). The fast SST response to ozone depletion in the MITgcm is
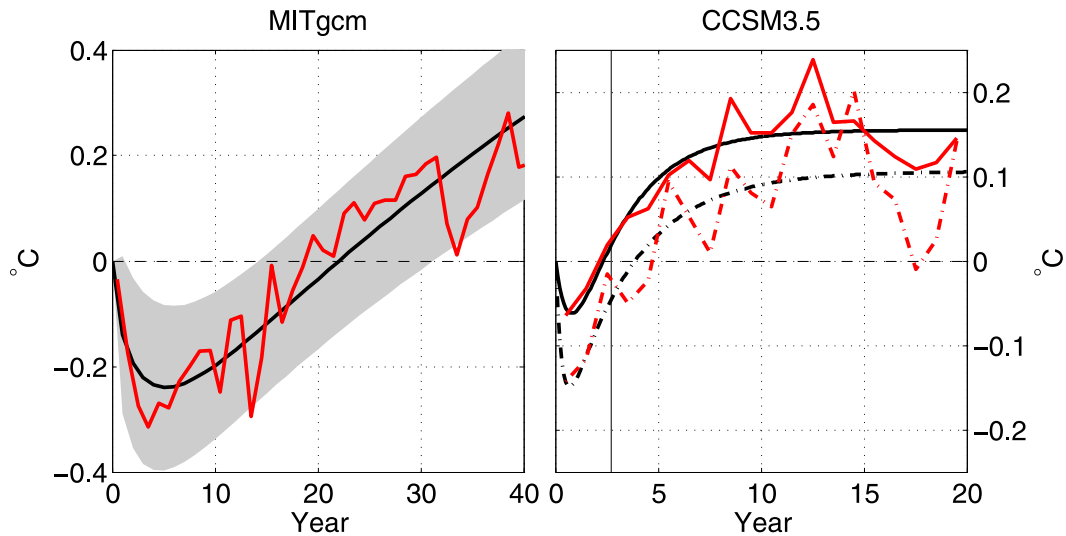
FIG. 6. Time evolution of the annual-mean ensemble-mean SST response (red) in (left) the MITgcm and (right) CCSM3.5. Solid lines correspond to an average between 70° and 50°S. In addition, for CCSM3.5, an average over the area occupied by the cold pole of the first year response (see Fig. 12 top, below) is shown with dashed–dotted lines. The solid black line indicates the mean of the best fitted curves, while the gray shading denotes uncertainties (see text for details). For the MITgcm, a 20-member ensemble is used over the 40 yr. For CCSM3.5, a 20-member ensemble mean is only available for the first 3 yr, after which only the ensemble mean comprises 6 members.

similar to the SST signature of a positive phase of the SAM in the same model [and similar to the signature found in observations and other models; Ciasto and Thompson (2008); Sen Gupta and England (2006)]. Because our setup is strongly zonally symmetric, the SST forcing is largely dominated by meridional Ekman advection. Note, however, that in more realistic configurations air–sea fluxes due to zonal asymmetries of the SAM pattern may be

important locally (Ciasto and Thompson 2008; Sallée et al. 2010).

2) THE SLOW RESPONSE

The Ekman current anomalies are divergent and drive anomalous upwelling south of 50°S and north of 35°S and an anomalous downwelling between these two latitudes. The Eulerian meridional overturning circulation (MOC)
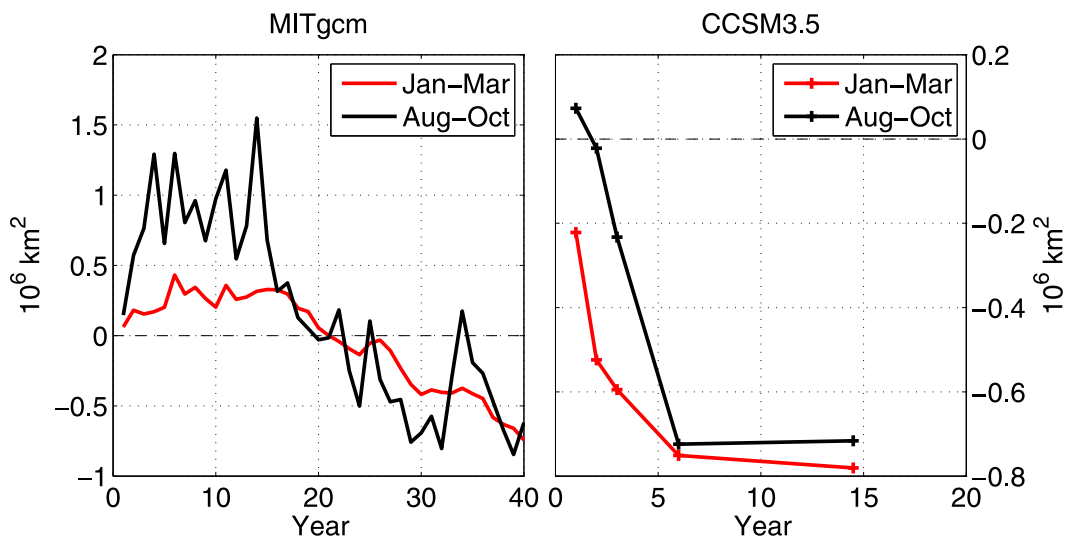

FIG. 7. Total sea ice area response (in 10^6 km^2) as a function of time in summer (January–March, red) and winter (August–October, black) in (left) the MITgcm and (right) CCSM3.5. Note that CCSM3.5 starts in September, so the first winter is an average of September–October only.
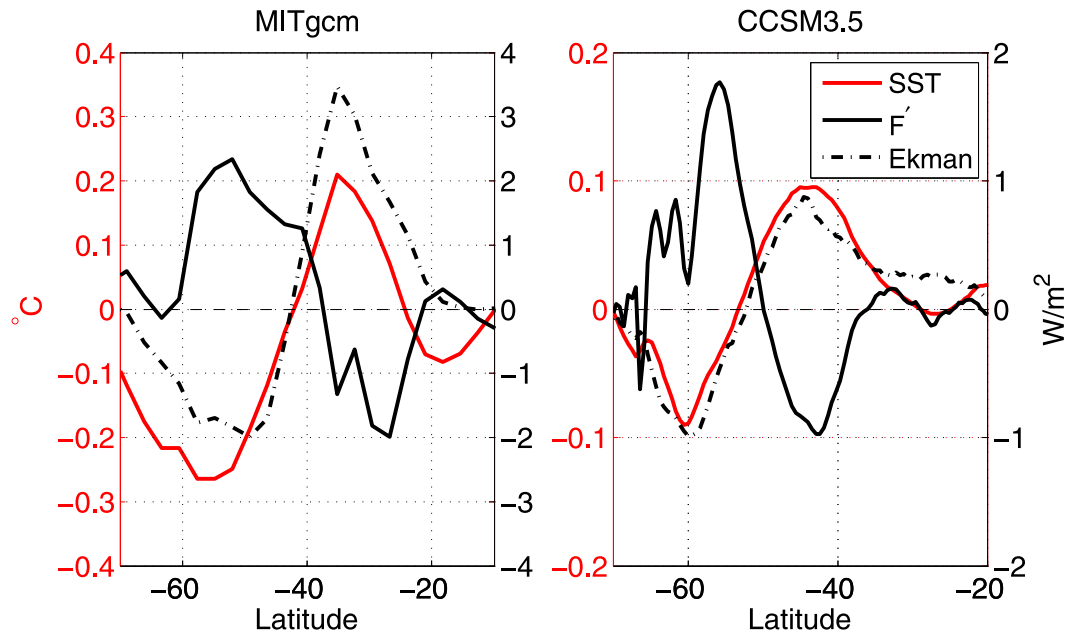
FIG. 8. Response of zonal-mean SST (°C, red), net air–sea flux F'_F (W m^{-2}, solid black), and horizontal advection at the surface, $-\rho_o c_p h_s v'_{res} \partial_y \overline{T}$ (W m^{-2}, dashed–dotted black) with $h_s = 30$ m. Fluxes are counted positive if they result in an SST increase. Results are shown for (left) the MITgcm experiment (averaged over years 2–3) and (right) CCSM3.5 (averaged over months 5–28). Note the different vertical scales in the two panels.

response consists then of two cells closely matching the surface wind stress anomalies (Fig. 9). South of 35°S where there are no meridional boundaries, the Eulerian MOC streamlines are vertical in the interior (as expected in the geostrophic limit) with return flows in the top and bottom Ekman layers. North of 35°S, meridional barriers allow for a middepth geostrophic return flow. At all latitudes, however, the strength of the Eulerian MOC just below the Ekman layer is very well approximated by the theoretical prediction $\tau_x/(\rho_o f)$ (on monthly and longer time scales) where τ_x is the zonal-mean zonal wind stress and f the Coriolis parameter (not shown).

Anomalies of the residual-mean circulation (sum of the Eulerian and parameterized eddy-induced circulations) are plotted in Fig. 10. Comparison of Figs. 10b and 9 (same averaging periods) shows that the residual-mean MOC anomalies are dominated by the Eulerian flow, retaining a clear connection to the pattern of surface wind anomalies. However, in analogy with the mean state balance, the eddy-induced MOC anomalies tend to oppose the wind-driven circulation anomalies, particularly south of 35°S where there are no meridional barriers. As a result, the residual-mean MOC anomalies are weaker than the wind-driven Eulerian MOC anomalies by as much as a factor of 2. On average over the band 70°–50°S, the residual-mean upwelling response is about 1 m yr^{-1}, compared to 1.5 m yr^{-1} for the Eulerian component (Fig. 11, top left). Note that the cancellation of the

Eulerian vertical velocity by the eddy-induced component is similar at all depths.

Because ocean temperature increases upward north of 55°S (see color contoured in Fig. 9, bottom), the downwelling and upwelling at these latitudes are expected to result in warming and cooling, respectively. However, the near-surface temperature stratification south of 55°S is reversed, with warmer water at depth because of the presence of seasonal sea ice (Fig. 9, bottom). Then upwelling south of this limit results in a warming. This is indeed observed in subsurface layers as shown in Fig. 10. Meridionally, the maximum temperature responses are clearly associated with branches of upwelling/downwelling. In the vertical, the temperature response peaks just below the mixed layer, around 100–200 m, where the summertime vertical stratification $\partial \overline{T}/\partial z$ is the largest. This is within reach of the wintertime deepening of the mixed layer that, on average in the band 70°–50°S, extends to about 150 m at its deepest. The cold SST response between 70° and 50°S stands out over years 1–5, when subsurface temperature anomalies remain weak (Fig. 10a). As time increases, however, the subsurface temperature anomalies grow larger and larger and eventually imprint themselves into the surface layer, through entrainment, so that by years 21–25, the cold SST anomaly has disappeared.

As shown in Fig. 10d, the time evolution of the subsurface (170 m deep) temperature response around 60°S is nearly linear over the first 40 yr. A best fit gives an
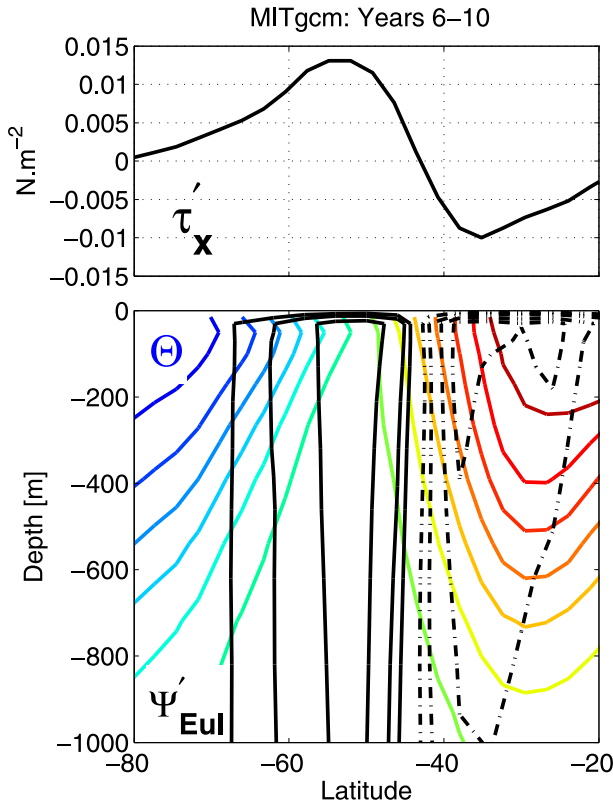
FIG. 9. (top) Annual-mean surface wind stress response ($N\,m^2$). (bottom) Annual-mean Eulerian MOC response [Sv ($1\,Sv \equiv 10^6\,m^3\,s^{-1}$), black] and potential temperature distribution in the control run (°C, color). The responses are averaged over years 6–10. The contour interval for temperature (color) is 2°C (from −2° to 24°C). The contours for the overturning (black) are −3, −2, −1, −0.5, +0.5, +1, +2, +3 Sv. Solid and dashed lines denote clockwise and counterclockwise circulations, respectively.

average warming rate of 0.017°C yr^{-1} (dashed black). This value is readily explained by the annual-mean residual upwelling anomaly w_{res} (~1 m yr^{-1}) acting on the mean temperature stratification $\partial\overline{T}/\partial z$ (~0.019°C m^{-1}) at this location. This confirms that the subsurface temperature response is well approximated by

$$\frac{\partial T'_{sub}}{\partial t} \simeq -w'_{res}\frac{\partial\overline{T}}{\partial z}. \qquad (2)$$

How much time is required for the upwelling of warm waters to compensate for the initial cold SST response around 60°S? The fast SST response at 60°S peaks at about −0.4°C (year 3, see Fig. 5, top). Assuming that subsurface temperatures are efficiently carried into the mixed layer through entrainment, the initial SST response would be cancelled when the subsurface temperature perturbation reaches +0.4°C. This takes about 20–25 yr (Fig. 10d), in good agreement with the SST evolution shown in Fig. 5.

After a couple of decades (Fig. 10c), the ocean has warmed south of 30°S at all depths (due to upwelling/downwelling collocated with positive and negative temperature stratification) and cooled north of 30°S (due to upwelling of cold water). This distribution resembles the averaged responses found by Sigmond and Fyfe (2010) and Bitz and Polvani (2012). The latter study identifies upwelling–downwelling anomalies driven by the SAM-like atmospheric perturbation as a primary driver of the temperature response. In addition, Bitz and Polvani (2012) shows (see their Fig. 3) that this effect is at work both at coarse (1°) and eddy-resolving (0.1°) resolutions in CCSM3.5. Although the relative importance of eddies and mean flow vertical advection depends on resolution, their result suggests that ocean eddies do not have a major influence on the quasi-equilibrium response. Note, however, this does not imply that eddies do not have an influence on the rate at which quasi-equilibrium response is approached (see below).

Two aspects of the temperature evolution deserve comment:

1) The fast SST response is driven primarily by anomalous horizontal rather than vertical advection. A scaling of these two terms is

$$\alpha = \frac{v'_{res}\overline{T}_y}{w'_{res}\overline{T}_z} \sim \frac{\overline{T}_y}{\overline{T}_z}\frac{L_y}{h_s}, \qquad (3)$$

where $\overline{T}_y$ is the meridional temperature gradient at the surface, $\overline{T}_z$ is the stratification just below the mixed layer, and L_y is the width of the upwelling zone (~20° for the band 50°–70°S). We assume that, at the scaling level, $v'_{ek}/w'_{ek} \sim v'_{res}/w'_{res}$. We find that α is about 15–30 (for $\overline{T}_z = -0.015 - 0.020$°C m^{-1}, $\overline{T}_y = 4 - 6 \times 10^{-6}$°C m^{-1}, and $h_s = 30$ m). It is large because the width of the upwelling zone is much greater than the depth of the horizontal flow ($L_y \gg h_s$ or equivalently, through volume conservation, $|v'_{ek}| \gg |w'_{ek}|$). Despite the fact that $\overline{T}_z \gg \overline{T}_y$, horizontal advection dominates. In subsurface layers, by contrast, there are no air–sea fluxes and little damping. Then, subsurface temperature anomalies induced by anomalous upwelling grow unabated over decades and are eventually imprinted into the surface layers through entrainment during the fall/winter deepening of the mixed layer.

2) The impact of (parameterized) eddies is significant in setting the subsurface warming rates. As shown above the residual-mean overturning anomalies are dominated by the Eulerian wind-driven component on yearly averages but are partially compensated by eddy-induced MOC anomalies. The anomalous Eulerian component is much larger than the annual
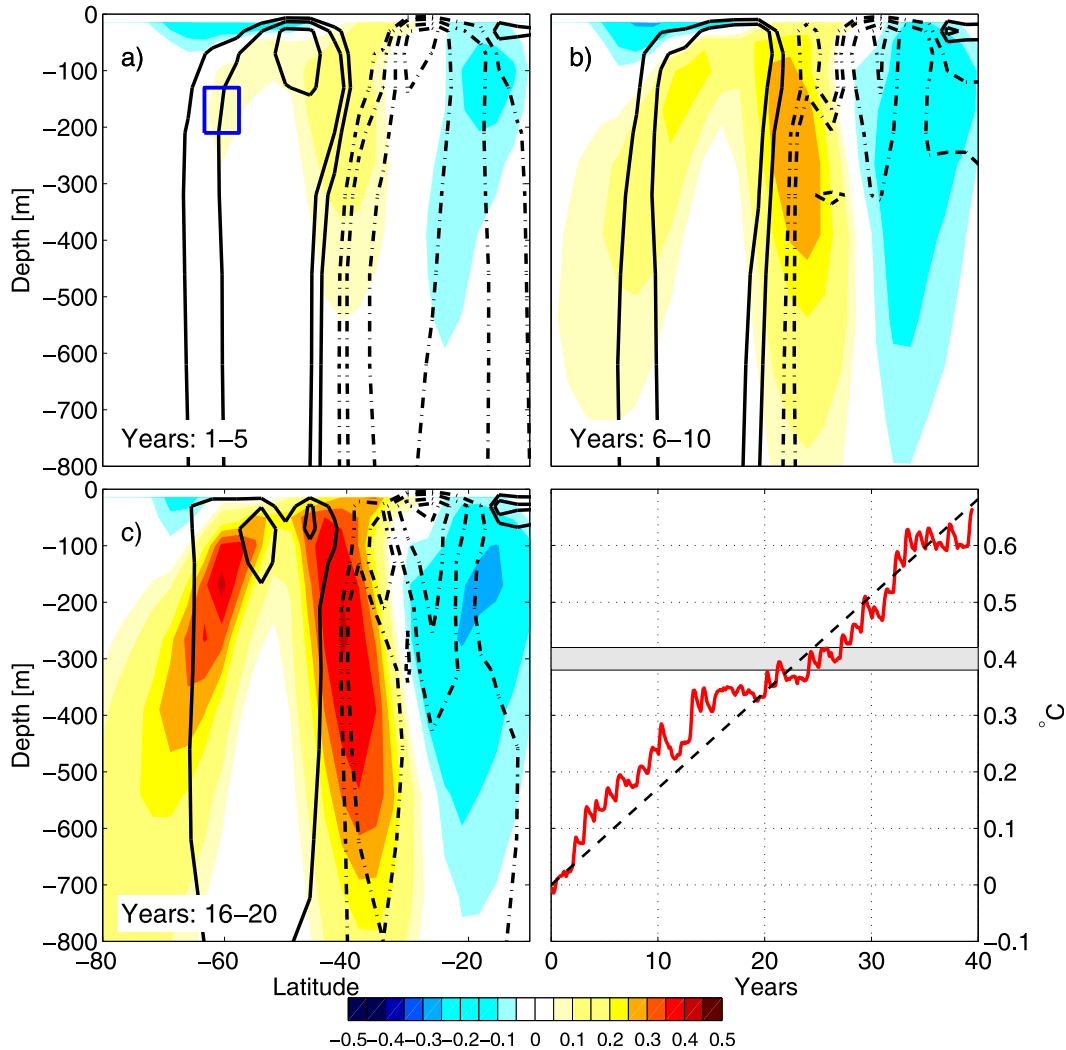
FIG. 10. (a)–(c) Residual-mean MOC response (black) and potential temperature response (colors, °C) averaged over 5-yr periods in the MITgcm. The contour intervals for the MOC are ±0.5, ±1, ±2 Sv, etc … Clockwise and anticlockwise circulations are denoted by solid and dashed lines, respectively. (d) Time series of potential temperature (red) averaged over the box shown in (a). The best-fit slope (dashed black) equals 0.017°C yr^{-1}. The gray shading indicates the magnitude of the fast (cold) SST response around 60°S.

mean during summer months when the anomalous surface wind stress peaks, but is vanishingly small in winter. By contrast, the eddy-induced circulation anomalies, which are proportional to the perturbations in isopycnal slope, are more steady. This is reflected in the yearly fluctuations superimposed on the slow increase of the subsurface temperature anomalies at 60°S shown in Fig. 10d. During summer, the wind forcing dominates and isotherms are lifted. During wintertime, the wind forcing disappears and only the eddy-induced MOC persists: isotherms are relaxed back toward their unperturbed position. In the annual mean, the Eulerian vertical advection dominates, but the rate of temperature increase in

subsurface layers is significantly affected by the eddy contribution. If the wind forcing was the only process acting, the rate of anomalous upwelling at 60°S would be 2 m yr^{-1}, twice as fast as the rate due to the anomalous residual flow (1 m yr^{-1}). Thus, the upwelling anomaly w'_{res} in Eq. (2) can be expressed as

$$w'_{\text{res}} = \delta w'_{\text{ek}} = \delta \left[\frac{\partial}{\partial y} \left(\frac{\tau'_x}{\rho_o f} \right) \right], \qquad (4)$$

where δ is an "eddy compensation" parameter that ranges from 1 (no eddy compensation) to 0 (exact eddy compensation). In the MITgcm experiments, $\delta = 0.3$–0.5 in the band on upwelling (70°–50°S) at
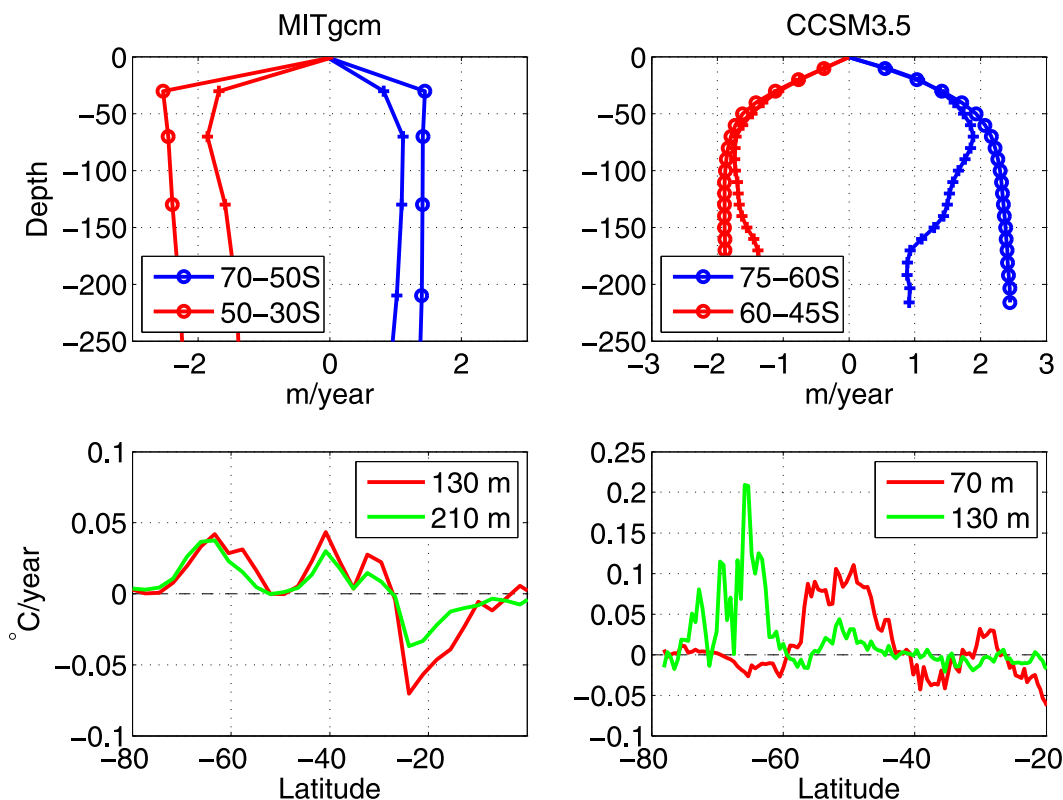
FIG. 11. For (left) MITgcm and (right) CCSM3.5: (top) Eulerian (circles) and residual-mean (crosses) vertical velocities (m yr^{-1}) averaged over the latitudinal bands dominated by upwelling (blue) and downwelling (red); (bottom) subsurface vertical advection tendencies $-w'_{res}\partial\overline{T}/\partial z$ (°C yr^{-1}). Note that the (top) boundaries of the latitudinal bands and (bottom) depths at which vertical advection peaks vary between models as indicated by insets. Note also that, in the bottom plots, the vertical scale for CCSM3.5 is larger than for MITgcm.

100–200-m depth. It is interesting that in the mean (i.e., control state) Eulerian and eddy-induced MOC also compensate roughly by this amount (see Marshall and Radko 2003).

In summary, we find that the warming of SST on long time scales in the band 70°–50°S is due to upwelling of warm water (primarily driven by Ekman divergence). The time to the SST reversal is well approximated by the time necessary for the subsurface warming to offset the initial cold SST response, about 20 years here. The long-term temperature response is consistent with previous findings and accounts for the retreat of sea ice in response to ozone depletion on long (multidecadal) time scales.

4. Ocean and sea ice response in CCSM3.5

a. Temperature and sea ice response

The response to ozone depletion in CCSM3.5 has many similarities with that found in the MITgcm, but also some important differences of detail. Of most significance is that the SST response again has two phases: first a dipole

response in the meridional direction followed by a widespread warming of the Southern Ocean, as in the MITgcm (cf. Figs. 12 and 4) CCSM3.5 has much more realistic geometry than the MITgcm configuration and so the initial SST response (similar to the modeled SST signature of a positive phase of the SAM) exhibits important zonal asymmetries, unlike the MITgcm (Fig. 12, top). In particular, the cold SST pole around 60°S is interrupted downstream of the Drake Passage where the warm pole extends across the ACC into the western part of the Weddell Sea. This feature is also found in the observed SST response to a positive phase of the SAM (see Ciasto and Thompson 2008) and corresponds to a region where air–sea heat fluxes, rather than Ekman currents, dominate the SST anomaly forcing. Note, however, that the SST response to ozone depletion in CCSM3.5 differs from the observed SAM-forced SST anomaly in some other aspects. For example, the negative pole in the Pacific sector is larger and extends farther equatorward.

As in the MITgcm experiment, over time the SST (and subsurface) responses morph into a widespread warming (Fig. 12, bottom). The transition between the two
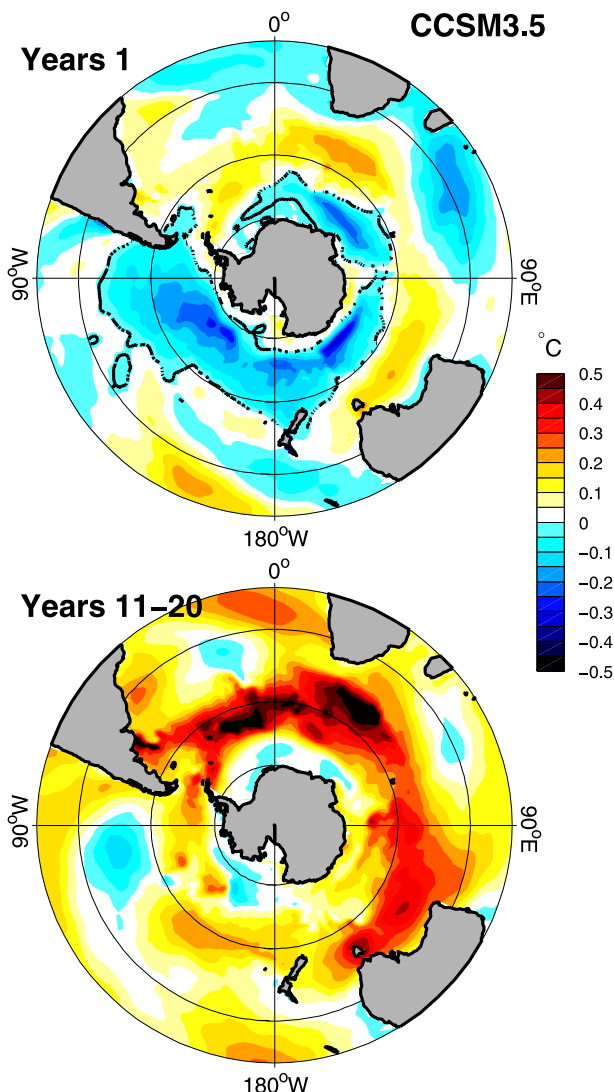
FIG. 12. Response of SST (°C) averaged over the (top) first year and (bottom) years 11–20 after an abrupt ozone depletion in the CCSM3.5.

phases, however, occurs much faster in CCSM3.5, after only 3–5 yr (Fig. 5, bottom). Around 60°S, between years 3 and 5, cold SST anomalies during summer (at the peak of the wind forcing) alternate with warm anomalies during winter. At 70°S, the cold SST response reappears during most summers for nearly two decades.

The amplitude of the SST response in CCSM3.5 is weaker than in the MITgcm, with peak values of ±0.3°C (cf. ±0.6°C in MITgcm), reflecting the difference in the surface wind response to ozone depletion in the two models. Largely due to the zonal asymmetries of the SST response in CCSM3.5, the zonal-mean initial response is only −0.2°C (Fig. 5, bottom) and averaged between 70° and 50°S it is only −0.05°C (Fig. 6, right, red solid). For

a meaningful comparison with the MITgcm, therefore, the SST evolution averaged over the area comprising the initial cold pole (see Fig. 12, top) is also shown in Fig. 6 (right, dashed red). According to this measure, the initial SST response is larger (−0.15°C) in magnitude and changes sign at a later time (5 yr) than in the zonal average. When comparing the two models, the initial cooling response in CCSM3.5 is also partially obscured by the warming trend that grows much more rapidly than in the MITgcm (see below). Despite these differences, the two phases of the SST response are clearly evident in Fig. 6 (right). After the sign reversal during years 3–5, the SST continues to increase for a few years more and appears to stabilize around 0.15°C after a decade or so. Note that only six ensemble member are available after 3 yr and so larger variability is evident. The appearance of a stationary state after 10 years may not be a robust feature.

The rapid transition between the two phases is also evident in the sea ice response. The sea ice area only increases during the first winter following the ozone hole inception (Fig. 7, right) while the summer sea ice area decreases sharply. The area of winter sea ice also eventually declines. The magnitude of the sea ice area decline in the slow phase of the two models is similar although the decline occurs about a decade sooner in CCSM3.5.

b. Role of ocean circulation on temperature evolution

The underlying dynamics of the SST evolution in CCSM3.5 is similar to that in the MITgcm although the magnitudes of key terms in the heat budget and implied time scales are different.

In the zonal mean, the initial SST anomaly dipole is largely explained by the anomalous Ekman response (Fig. 8, right). To match the short-lived initial response, the forcing terms and SST anomalies in Fig. 8 (right) are averaged over 2 years. The Ekman forcing term (and the SST response) are about half those found in the MITgcm. The air–sea flux anomalies act to damp the SST response at all latitudes. The air–sea flux anomalies and Ekman forcing again tend to balance each other. There is one noticeable exception between 60° and 50°S where the air–sea flux term is larger in magnitude than the Ekman term. Here, the air–sea flux warms the surface faster than it is cooled by Ekman advection. More detailed analysis reveals that this is a result of an increased shortwave absorption at the surface due to a decrease of the cloud fraction (not shown).

The other important mechanism identified in the MITgcm experiment is the wind-driven subsurface warming below the initial cold SST anomaly. Figure 11 (right) shows the vertical velocity anomalies and the resulting tendency $-w'_{res}\partial\overline{T}/\partial z$ in CCSM3.5 (at two depths where the values are largest). South of 60°S, the

TABLE 1. Parameters of the simple model estimated by fitting Eqs. (8) and (9) to the SST and subsurface temperature time series diagnosed in the MITgcm and CCSM3.5 ($h_s = 30$ m). The model time series and fitted curves are shown in Fig. 13. The temperatures responses are averaged over 70°–50°S for the MITgcm and over the initial cold SST response for CCSM3.5. Note that λ_F and $\tilde{F}_F$ are the same physical quantities as λ and $\tilde{F}$, but expressed in W m^{-2} K^{-1} and W m^{-2}, respectively, assuming a mixed layer depth h_s of 30 m for both models.

	Air–sea damping		Atmospheric forcing		λ_{sub}^{-1}	Λ_e^{-1}	$-w'_{res}\partial_z\overline{T}_{sub}$
	λ^{-1} yr	λ_F W m^{-2} K^{-1}	$\tilde{F}$ °C yr^{-1}	$\tilde{F}_F$ W m^{-2}	yr	yr	°C yr^{-1}
MITgcm	2.6	1.5	−0.18	−0.7	78	1.5	0.014
CCSM3.5	0.59	6.7	−0.27	−1.1	6.8	0.36	0.027

anomalous Ekman divergence drives upwelling in a region where the temperature decreases toward the surface (Fig. 11, top right). As in the MITgcm, this results in a positive tendency. Note that w'_{res} is larger at 70 than at 130-m depth, but that the temperature tendency at 70 m is much smaller because this level lies within the mixed layer and the temperature stratification is weak. North of 60°S, the mixed layer is shallower and strong tendencies are found closer to the surface. The large positive tendency, of 0.1°C yr^{-1}, centered on 50°S is due to the downwelling of warm waters while the large negative tendency around 40°S is due to the upwelling of cold water.

The vertical advection tendencies in CCSM3.5 are significantly larger than in the MITgcm (Fig. 11, bottom, note the different vertical scales in the two panels), typically by a factor of 2 in the band 70°–50°S (see also estimated values in Table 1 and section 5 below).

Comparing the annual- and zonal-mean wind stress responses in the MITgcm and CCSM3.5 (Fig. 3), it appears that 1) the responses of the two models are shifted in the meridional direction, one with respect to the other (surface wind anomaly peaks around 65°S in CCSM3.5 but around 55°S in the MITgcm); and 2) the meridional scale of the wind change in CCSM3.5 is smaller than in the MITgcm. This leads to stronger wind curl anomalies and, hence, larger Eulerian upwelling rates. In addition, the cancellation of the wind-driven upwelling by the eddy-induced vertical velocity differs between the two models. In contrast with the MITgcm (Fig. 11, top left), eddy-induced contributions to upwelling rates are very small compared to the Eulerian mean down to 100-m depth in CCSM3.5. The difference in the degree of eddy cancellation between models may be due to differences in the eddy parameterization scheme: the MITgcm uses a constant eddy coefficient while CCSM3.5 uses a temporally and spatially variable eddy coefficient [following Ferreira et al. (2005), see their section 2]. The combination of a larger wind-driven upwelling and a weaker eddy cancellation largely explains the stronger warming tendencies seen in CCSM3.5 (Fig. 11, bottom), and as we shall see, is a major factor in the shorter cross-over time from cooling to warming.

5. Discussion and development of a simplified model

The discussion in sections 3 and 4 has enabled us to identify common robust mechanisms of warming and cooling in the two models. Here we use the insights gained to present a simplified model of the response of the ocean to SAM forcing, which exposes those processes in a transparent way.

a. Formulation

To aid our discussion, motivated by diagnostics of our two coupled models, we present the following simple model of the temperature response:

$$\frac{\partial T'}{\partial t} = -v'_{res}\frac{\partial \overline{T}}{\partial y} + F'_a - \lambda T' + \Lambda_e T'_{sub}, \qquad (5)$$

$$\frac{\partial T'_{sub}}{\partial t} = -w'_{res}\frac{\partial \overline{T}_{sub}}{\partial z} - \lambda_{sub} T'_{sub}, \qquad (6)$$

where T' is the SST response, T'_{sub} is the subsurface temperature response (imagined to be typical of the seasonal thermocline), and Λ_e represents the entrainment time scale of the subsurface temperature into the mixed layer. The subsurface temperature is assumed to adjust on a time scale λ_{sub}^{-1}, which encapsulates complex dynamics relevant to the equilibrium response and adjustment of the SO seasonal thermocline. The overbar denotes the climatological state of the control run, and the prime is the perturbation in response to the anomalous wind forcing. In the absence of a dynamical response in the ocean interior (w'_{res}) and/or of an influence of the interior on the surface layer ($\Lambda_e = 0$), the SST anomaly equation reduces to

$$\frac{\partial T'}{\partial t} = \tilde{F} - \lambda T', \qquad (7)$$

where $\tilde{F} = F'_a - v'_{res}\partial_y\overline{T}$ is the atmospheric forcing of the mixed layer by air–sea flux and Ekman current anomalies. This is the classical model of midlatitude SST variability (Frankignoul and Hasselmann 1977).

We are interested in the response to a step function wind change. Assuming a constant atmospheric forcing (v'_{res}, w'_{res}, $F'_a = $ const) for $t > 0$, solutions are given by

$$T' \simeq \frac{\tilde{F}}{\lambda}(1 - e^{-\lambda t}) + \frac{\Lambda_e}{\lambda} T'_{sub}, \qquad (8)$$

$$T'_{sub} = \frac{-w'_{res}\partial_z \overline{T}_{sub}}{\lambda_{sub}}(1 - e^{-\lambda_{sub}t}), \qquad (9)$$

in the limit $\lambda_{sub} \ll \lambda$ appropriate to our models. The subsurface temperature in (9) grows monotonically on a time scale λ_{sub}^{-1}. The SST response in (8) is the sum of two exponential functions: one captures the fast response driven by mixed layer dynamics while the second one, $\Lambda_e/\lambda T'_{sub}$, is driven by the slow ocean interior dynamics. Note that for $t \ll \lambda_{sub}$, T'_{sub} increases linearly at a rate given by $-w'_{res}\partial_z \overline{T}_{sub}t$ as found in the coupled GCMs. Parameters obtained from a best fit of Eqs. (8) and (9) to the SST and subsurface temperature evolution in both the MITgcm and CCSM3.5 are given in Table 1. The best-fit curves are shown in Fig. 13 (solid) with their fast and slow components (dashed). It is important to emphasize that the response to a step function in the classical model in (7) reduces to the fast component if the ocean is passive (lower dashed curves in Fig. 13). Thus, both coupled GCMs depart significantly from the Frankignoul and Hasselmann (1977) classical model, attesting to the active role of ocean circulation in modulating the SST response.

The fitted parameters in Table 1 are clearly estimates and depend on the underlying assumptions of the simple model in Eqs. (5) and (6). They nonetheless provide useful insights in to processes at work and the differences between the two GCMs. There are two key differences between the coupled models that we will now discuss in turn: air–sea fluxes–damping rates and the response of the interior ocean.

b. Air–sea interactions

The first difference that stands out is in the strength of the air–sea heat exchanges. The atmospheric-driven forcing $\tilde{F}_F$ ($=\rho_o C_p h_s \tilde{F}$ in W m^{-2}) is -0.7 W m^{-2} in the MITgcm and -1.1 W m^{-2} in CCSM3.5 (average values in the band 70°–50°S). Comparison with Fig. 8 suggests that $\tilde{F}_F$ largely comprises the anomalous Ekman advection in the MITgcm, but is significantly amplified by F'_a in CCSM3.5 (possibly because of the larger zonal asymmetries in CCSM3.5). Changes in the atmospheric circulation (a positive SAM here) and ozone concentration are both expected to affect the radiation reaching the surface. Recently, Grise et al. (2013) showed that ozone depletion could alter the top-of-the-atmosphere

longwave and shortwave fluxes by a few watts per meter squared (W m^{-2}) in the band 70°–40°S through a modulation of the cloud fraction. A similar impact on the surface fluxes is anticipated (regardless of the ocean response) although we cannot discriminate between the MITgcm and CCSM3.5 in this respect. In addition, the estimated heat flux feedback $\lambda_F = \lambda/(\rho_o C_p h_s)$ is much larger in CCSM3.5 than in the MITgcm (6.7 and 1.5 W m^{-2} K^{-1}, respectively). We do not have good estimates of the heat flux feedback in the Southern Ocean. Frankignoul et al. (2004) find that λ_F is typically about 15–20 W m^{-2} K^{-1} at the local scale in the midlatitudes, but tends to decrease significantly at the basin scale ($\sim$10 W m^{-2} K^{-1}) in the North Atlantic–Pacific. It is expected to decrease further at the global scale of the SO. Again, zonal asymmetries in CCSM3.5 probably contribute to the difference between the two models, enhancing air–sea contrast and damping rates as air parcels move above the Southern Ocean. Cloud and sea ice feedbacks are also likely contributors. Despite the factor of 4 difference between the CCSM3.5 and MITgcm heat flux feedback, neither can be ruled out as unrealistic. Thus, it appears that the air–sea heat interactions (forcing and damping) are significantly more intense in CCSM3.5 than in the MITgcm.

c. Response of the interior ocean

The Frankignoul and Hasselmann (1977) model is modified by ocean interior dynamics in our simple model. In the limit $t \ll \lambda_{sub}^{-1}$, the SST response in (8) becomes

$$T' \simeq \frac{\tilde{F}}{\lambda}(1 - e^{-\lambda t}) - \frac{\Lambda_e}{\lambda}w'_{res}\partial_z \overline{T}_{sub}t. \qquad (10)$$

The time t_r at which the SST changes sign, $T'(t_r) = 0$, then depends on λ but no longer on λ_{sub}. Further assuming $\lambda^{-1} \ll t \ll \lambda_{sub}^{-1}$, t_r simplifies to

$$t_r \simeq \frac{1}{\Lambda_e}\frac{-\tilde{F}}{-w'_{res}\partial_z \overline{T}_{sub}} = \frac{1}{\Lambda_e}\frac{v'_{res}\partial_y \overline{T} - F'_a}{-w'_{res}\partial_z \overline{T}_{sub}}. \qquad (11)$$

Note that the above expression does not apply well to the CCSM3.5 case where t_r is only a factor of 2 smaller than λ_{sub}. Nonetheless, Eq. (11) points to the key role of residual circulation in driving the change of sign. The larger v'_{res}, the longer the transition (through a larger initial cooling of SST) while the larger w'_{res}, the shorter the transition (through increases of the subsurface warming rate). As pointed out in Eq. (4) (and Fig. 11), the residual upwelling flow results from a cancellation (by a factor of δ) of the wind-driven upwelling by the (parameterized) eddy-induced downwelling. However,
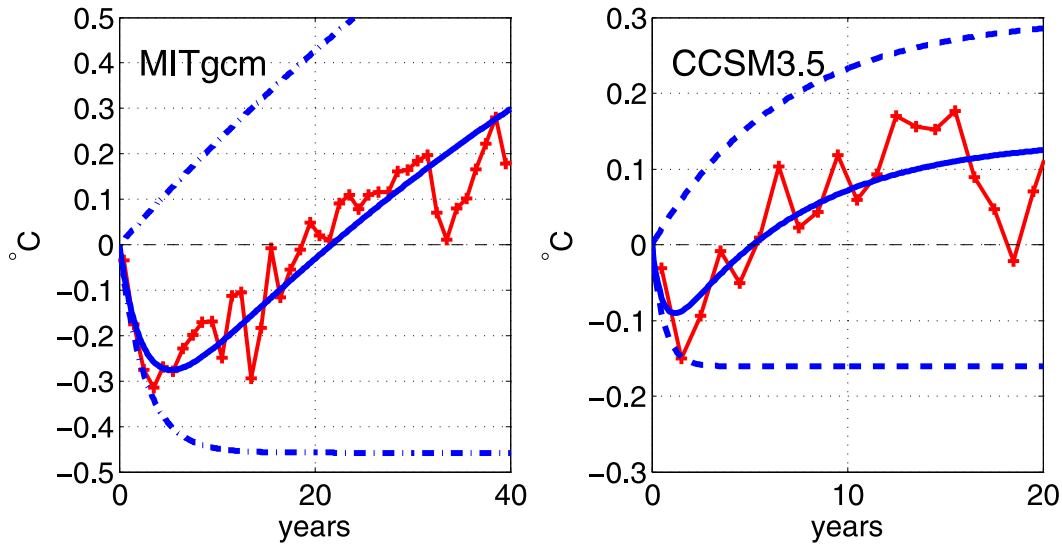
FIG. 13. Best-fit (solid blue) of Eq. (8) to the CFR of the SST evolution (red, averaged over 70°–50°S for the MITgcm and over the initial cold SST response for CCSM3.5) in (left) the MITgcm and (right) CCSM3.5. The slow and fast components of the best fit are shown in dashed lines.

the cancellation of the Ekman horizontal flow by the eddy-induced circulation is relatively weak in comparison with that of the vertical flow. This is because the Eulerian and eddy-induced streamfunctions do not have the same vertical distribution. The Eulerian streamfunction is constant over the fluid column and decays to zero at the surface within the Ekman layer (~30 m) (i.e., the horizontal flow is very confined vertically; Fig. 9). In contrast, the eddy-induced flow near the surface is spread over a deeper layer, of about 200 m. This mismatch between the vertical scales of the two MOC components is observed in eddy-resolving simulations (see Abernathey et al. 2011; Morrison and Hogg 2013) and should not be considered an erroneous effect of the Gent and McWilliams eddy parameterization employed in the coupled GCMs (although the use of a tapering scheme in the GM scheme may have an influence). This suggests that $w'_{res} = \delta w'_{ek}$ and $v'_{res} \simeq v'_{ek}$ is a better choice in which case:

$$t_r \simeq \frac{1}{\Lambda_e} \frac{v'_{ek} \partial_y \overline{T} - F'_a}{-\delta w'_{ek} \partial_z \overline{T}_{sub}}. \qquad (12)$$

In the limit of perfect eddy compensation ($\delta = 0$), t_r would go to infinity as there would be no subsurface upwelling and warming and the initial cold SST response would persist indefinitely. In the limit of no eddy compensation ($\delta = 1$), the transition t_r would be more rapid. Equation (12) emphasizes that the eddy processes (vertical structure, magnitude) may be key in determining the time scale of the SST reversal.

Finally, we point to the role of the entrainment time scale Λ_e^{-1}, which modulates the imprint of the subsurface

temperature onto the SST. It is shorter in CCSM3.5 than in the MITgcm, 0.4 and 1.5 yr, respectively (Table 1). The shorter CCSM3.5 time scale (promoting a shorter transition time t_r) could possibly be due to the shallower depth of the peak subsurface tendencies (see Fig. 11) or the use of a mixed layer scheme and higher vertical resolution. In both models however, the ratio λ/Λ_e which appears in Eq. (8), is about 0.6 and the warming trend of the SST mimics that of the subsurface temperature (Fig. 13).

6. Conclusions

In this study, we have explored the ocean and sea ice response to ozone depletion in two coupled GCMs. The ozone depletion is imposed as a step function and we compute the transient response of the coupled system to this perturbation. As in other studies, the surface westerly winds shift poleward and strengthen during summer in response to ozone depletion; this atmospheric response is similar to the positive phase of the SAM.

The first key result of our study is that the SST response to this wind perturbation in the Southern Ocean has two phases (see Fig. 1 for a schematic). The fast response occurs on monthly time scale following the SAM-like wind perturbation, but also builds up over a few years. It is mediated by mixed layer dynamics and air–sea interaction. It consists of a dipole, with a cooling south of the ACC (where the surface wind increases) and a warming where surface westerly winds weaken (around 35°S) (Fig. 1, left). This response is primarily driven by anomalous Ekman advection with air–sea heat

interactions acting as a damping. The slow response is due to interior ocean dynamics. The northward Ekman flow at 70°–50°S drives upwelling south of the ACC, which brings warm water to the surface. At these latitudes where sea ice expands seasonally, the water column is stratified by salinity and cold water at the surface lies over warm water below. On long (multiyear) time scales, this warmth can be entrained into the mixed layer and counteracts the initial SST cooling (Fig. 1, right). Eventually, the SST response to ozone depletion is a widespread warming of the SO.

The second key result of our study is that there is no inconsistency between inferences based on SAM–SST correlations and modeling studies of the SO response to ozone depletion. Sigmond and Fyfe (2010) and Bitz and Polvani (2012) found that ozone depletion drives a warming of the SO and sea ice loss in coupled GCMs. The SST–sea ice signatures of the positive phase of the SAM, however, suggest that ozone depletion through its surface wind impact should generate a SST cooling around Antarctica and a sea ice expansion (Goosse et al. 2009). These two conclusions are reconciled within one framework by our results showing a two-time-scale response to ozone depletion.

Finally, a related overall outcome is that ozone depletion could drive a transient expansion of the sea ice cover around Antarctica that could have contributed to the observed sea ice expansion of the last three decades (Parkinson and Cavalieri 2012). In both GCMs used here, the initial sea ice response to an abrupt ozone depletion is one of expansion, followed by a contraction of the sea ice cover as the surface warms. This long-term response is consistent with findings by Sigmond and Fyfe (2010) and Bitz and Polvani (2012). However, the true (time varying) influence of ozone depletion on the sea ice extent will critically depend on the time scale of the transition from cooling to warming. One expects that in a model with a short transition time scale such as CCSM3.5, prescribing the time history of the ozone depletion would not result in a significant sea ice expansion [consistent with results of Smith et al. (2012), albeit obtained with CCSM4]. On the contrary, in a model with a long transition time scale such as the MITgcm, a transient SST cooling and sea ice expansion is obtained in response to the historical variations of the ozone hole (work in progress).

An important corollary of this study is that analysis of the relationship between sea ice cover and SAM changes in observations may require more sophisticated tools than previously used in the literature (e.g., simultaneous correlations or trends). In a recent study, for example, Simpkins et al. (2012) computed the sea ice cover trends that are linearly congruent with the SAM

during summer. To do this, they regressed sea ice anomalies onto the detrended SAM index, and then multiplied the resulting regression coefficients by the trend in the SAM. Such an approach effectively assumes that there is a single relationship between SAM and sea ice cover changes that applies on all times scales, or, equivalently that there is only one (fast) time-scale response. Simpkins et al. (2012) (and others, see references therein) found, using such congruency analysis, that the SAM trends explain less 15% of the observed sea ice trends. This is not surprising in the light of our results: we do not expect that the simultaneous (3 month averaged) relationship between SAM and sea ice cover would capture their relationship on long multidecadal trends. Therefore, we argue that such low congruency obtained in observations does not rule out a dynamical link between SAM and sea ice trends of the past three decades. A more accurate exploration of the SAM–sea ice link needs to account for the two-time-scale response.

Although the two-time-scale SST response is a robust result seen in the two GCMs studied here and the mechanisms of this response are largely similar in the two GCMs, the time scale of the transition between the cold and warm SST phases around Antarctica is poorly constrained, being 20 yr in the MITgcm and 3–5 yr in CCSM3.5.

Two main sources of uncertainties have been identified: the nature of the air–sea interaction and the response of the interior ocean. Air–sea heat fluxes are partly driven by atmospheric changes (notably changes in wind and cloud effects) and partly by rates of damping of the SST anomaly once it is created. Parameterized mesoscales eddies control the effective rate of subsurface warming by partially canceling the wind-driven upwelling. We emphasize that in both GCMs, eddy processes are parameterized. Eddy-resolving simulations have shown that such cancellation is difficult to capture in parameterization schemes (e.g., Hallberg and Gnanadesikan 2006; Abernathey et al. 2011). More studies are required to better quantify these processes, to constrain the transition time scale using coupled GCMs, process studies, and observations.

Despite the above caveats, our results robustly demonstrate that the Southern Ocean responds to wind on multiple time scales, reconciling previously contradicting views. Importantly, regardless of the true time scale of transition between the fast and slow phases, our results highlight the need to revise the classical model of extratropical air–sea interactions for the Southern Ocean to account for the interior ocean dynamics.

ozone hole on the Southern Hemisphere climate. Funding for CB was provided by the National Science Foundation (NSF PLR-1341497).

APPENDIX

The MITgcm

All components use the same cubed-sphere grid at a low resolution C24, yielding a resolution of 3.75° at the equator (Adcroft et al. 2004). The cubed-sphere grid avoids problems associated with the converging meridian at the poles and ensures that the model dynamics at the poles are treated with as much fidelity as elsewhere.

The atmospheric physics is of "intermediate" complexity, based on the "SPEEDY" scheme (Molteni 2003) at low vertical resolution (five levels: one in the stratosphere, three in the troposphere, and one in the boundary layer). Briefly, it comprises a four-band radiation scheme, a parameterization of moist convection, diagnostic clouds, and a boundary layer scheme. The 3-km-deep, flat-bottomed ocean model has 15 vertical levels, increasing from 30 m at the surface to 400 m at depth. The background vertical diffusion is uniform and set to $3 \times 10^{-5} \, \mathrm{m^2 \, s^{-1}}$.

The sea ice model is based on Winton (2000)'s 2½-layer thermodynamic model with prognostic ice fraction, snow, and ice thickness (employing an energy-conserving formulation). The land model is a simple 2-layer model with prognostic temperature, liquid groundwater, and snow height. There is no continental ice. The seasonal cycle is represented (with a 23.5° obliquity and zero eccentricity), but there is no diurnal cycle.

Finally, as discussed by Campin et al. (2008), the present coupled ocean–sea ice–atmosphere model achieves perfect (machine accuracy) conservation of freshwater, heat, and salt during the extended climate simulation. This is made possible by the use of the rescaled height coordinate $z^{\star}$ (Adcroft and Campin 2004), which allows for a realistic treatment of the sea ice–ocean interface. This property is crucial to the fidelity and integrity of the coupled system. The setup is identical to that used in Ferreira et al. (2010, 2011) and very similar to that of Marshall et al. (2007) and Enderton and Marshall (2009) [see Ferreira et al. (2010) for key differences].

REFERENCES

Abernathey, R., J. Marshall, and D. Ferreira, 2011: The dependence of Southern Ocean meridional overturning on wind stress. *J. Phys. Oceanogr.,* **41,** 2261–2278, doi:10.1175/JPO-D-11-023.1.

Adcroft, A., and J.-M. Campin, 2004: Re-scaled height coordinates for accurate representation of free-surface flows in ocean circulation models. *Ocean Modell.,* **7,** 269–284, doi:10.1016/j.ocemod.2003.09.003.

——, ——, C. Hill, and J. Marshall, 2004: Implementation of an atmosphere–ocean general circulation model on the expanded spherical cube. *Mon. Wea. Rev.,* **132,** 2845–2863, doi:10.1175/MWR2823.1.

Bitz, C. M., and L. M. Polvani, 2012: Antarctic climate response to stratospheric ozone depletion in a fine resolution ocean climate model. *Geophys. Res. Lett.,* **39,** L20705, doi:10.1029/2012GL053393.

Bryan, F. O., P. R. Gent, and R. Tomas, 2014: Can Southern Ocean eddy effects be parameterized in climate models? *J. Climate,* 27, 411–425, doi:10.1175/JCLI-D-12-00759.1.

Campin, J.-M., J. Marshall, and D. Ferreira, 2008: Sea ice-ocean coupling using a rescaled vertical coordinate z^*. *Ocean Modell.,* **24,** 1–14, doi:10.1016/j.ocemod.2008.05.005.

Ciasto, L. M., and D. W. J. Thompson, 2008: Observations of large-scale ocean–atmosphere interaction in the Southern Hemisphere. *J. Climate,* **21,** 1244–1259, doi:10.1175/2007JCLI1809.1.

Cionni, I., and Coauthors, 2011: Ozone database in support of CMIP5 simulations: Results and corresponding radiative forcing. *Atmos. Chem. Phys. Discuss.,* **11,** 10875–10933, doi:10.5194/acpd-11-10875-2011.

Comiso, J. C., and F. Nushio, 2008: Trends in the sea ice cover using enhanced and compatible AMSR-E, SSM/I, and SMMR data. *J. Geophys. Res.,* **113,** C02S07, doi:10.1029/2007JC004257.

Danabasoglu, G., and J. Marshall, 2007: Effects of vertical variations of thickness diffusivity in an ocean general circulation model. *Ocean Modell.,* **18,** 122–141, doi:10.1016/j.ocemod.2007.03.006.

Dee, D. P., and Coauthors, 2011: The ERA-Interim reanalysis: Configuration and performance of the data assimilation system. *Quart. J. Roy. Meteor. Soc.,* **137,** 553–597, doi:10.1002/qj.828.

Enderton, D., and J. Marshall, 2009: Explorations of atmosphere–ocean–ice climates on an aquaplanet and their meridional energy transports. *J. Atmos. Sci.,* **66,** 1593–1611, doi:10.1175/2008JAS2680.1.

Ferreira, D., J. Marshall, and P. Heimbach, 2005: Estimating eddy stresses by fitting dynamics to observations using a residual mean ocean circulation model and its adjoint. *J. Phys. Oceanogr.,* **35,** 1891–1910, doi:10.1175/JPO2785.1.

——, ——, and J.-M. Campin, 2010: Localization of deep water formation: Role of atmospheric moisture transport and geometrical constraints on ocean circulation. *J. Climate,* **23,** 1456–1476, doi:10.1175/2009JCLI3197.1.

——, ——, and B. Rose, 2011: Climate determinism revisited: Multiple equilibria in a complex climate model. *J. Climate,* **24,** 992–1012, doi:10.1175/2010JCLI3580.1.

Frankignoul, C., and K. Hasselmann, 1977: Stochastic climate models. Part II: Application to sea-surface temperature anomalies and thermocline variability. *Tellus,* **29A,** 289–305, doi:10.1111/j.2153-3490.1977.tb00740.x.

——, E. Kestenare, M. Botzet, A. F. Carril, H. Drange, A. Pardaens, L. Terray, and R. Sutton, 2004: An intercomparison between the surface heat flux feedback in five coupled models, COADS and the NCEP reanalysis. *Climate Dyn.,* **22,** 373–388, doi:10.1007/s00382-003-0388-3.

Gent, P. R., and J. C. McWilliams, 1990: Isopycnic mixing in ocean circulation models. *J. Phys. Oceanogr.,* **20,** 150–155, doi:10.1175/1520-0485(1990)020<0150:IMIOCM>2.0.CO;2.

——, S. G. Yeager, R. B. Neale, S. Levis, and D. A. Bailey, 2010: Improvements in half degree atmosphere/land version of the CCSM. *Climate Dyn.,* **34,** 819–833, doi:10.1007/s00382-009-0614-8.

Gillett, N. P., and D. W. J. Thompson, 2003: Simulation of recent southern hemisphere climate change. *Science,* **302,** 273–275, doi:10.1126/science.1087440.

Goosse, H., W. Lefebvre, A. de Montety, E. Crespin, and A. H. Orsi, 2009: Consistent past half-century trends in the atmosphere, the sea ice and the ocean at high southern latitudes. *Climate Dyn.,* **33,** 999–1016, doi:10.1007/s00382-008-0500-9.

Grise, K. M., L. M. Polvani, G. Tselioudis, Y. Wu, and M. D. Zelinka, 2013: The ozone hole indirect effect: Cloud-radiative anomalies accompanying the poleward shift of the eddy-driven jet in the southern hemisphere. *Geophys. Res. Lett.,* **40,** 3688–3692, doi:10.1002/grl.50675.

Hall, A., and M. Visbeck, 2002: Synchronous variability in the Southern Hemisphere atmosphere, sea ice, and ocean resulting from the annular mode. *J. Climate,* **15,** 3043–3057, doi:10.1175/1520-0442(2002)015<3043:SVITSH>2.0.CO;2.

Hallberg, R., and A. Gnanadesikan, 2006: The role of eddies in determining the structure and response of the wind-driven Southern Hemisphere overturning: Results from the Modeling Eddies in the Southern Ocean (MESO) project. *J. Phys. Oceanogr.,* **36,** 2232–2252, doi:10.1175/JPO2980.1.

Kiehl, J. T., T. L. Schneider, R. W. Portmann, and S. Solomon, 1999: Climate forcing due to tropospheric and statospheric ozone. *J. Geophys. Res.,* **104,** 31 239–31 254, doi:10.1029/1999JD900991.

Kirtman, B. P., and Coauthors, 2012: Impact of ocean model resolution on CCSM climate simulations. *Climate Dyn.,* **39,** 1303–1328, doi:10.1007/s00382-012-1500-3.

Klinger, B. A., J. Marshall, and U. Send, 1996: Representation of convective plumes by vertical adjustment. *J. Geophys. Res.,* **101,** 18 175–18 182, doi:10.1029/96JC00861.

Lefebvre, W., and H. Goosse, 2008: Analysis of the projected regional sea-ice changes in the Southern Ocean during the twenty-first century. *Climate Dyn.,* **30,** 59–76, doi:10.1007/s00382-007-0273-6.

——, ——, R. Timmermann, and T. Fichefet, 2004: Influence of the Southern Annular Mode on the sea–ice system. *J. Geophys. Res.,* **109,** C09005, doi:10.1029/2004JC002403.

Marshall, G. J., 2003: Trends in the southern annular mode from observations and reanalysis. *J. Climate,* **16,** 4134–4143, doi:10.1175/1520-0442(2003)016<4134:TITSAM>2.0.CO;2.

——, P. A. Stott, J. Turner, W. B. Connolley, J. C. King, and T. A. Lachlan-Cope, 2004: Causes of exceptional atmospheric circulation changes in the Southern Hemisphere. *Geophys. Res. Lett.,* **31,** L14205, doi:10.1029/2004GL019952.

Marshall, J., and T. Radko, 2003: Residual mean solutions for the Antarctic Circumpolar Current and its associated overturning circulation. *J. Phys. Oceanogr.,* **33,** 2341–2354, doi:10.1175/1520-0485(2003)033<2341:RSFTAC>2.0.CO;2.

——, A. Adcroft, C. Hill, L. Perelman, and C. Heisey, 1997a: A finite-volume, incompressible Navier–Stokes model for studies of the ocean on parallel computers. *J. Geophys. Res.,* **102,** 5753–5766, doi:10.1029/96JC02775.

——, C. Hill, L. Perelman, and A. Adcroft, 1997b: Hydrostatic, quasi-hydrostatic, and nonhydrostatic ocean modeling. *J. Geophys. Res.,* **102,** 5733–5752, doi:10.1029/96JC02776.

——, A. Adcroft, J.-M. Campin, C. Hill, and A. White, 2004: Atmosphere–ocean modeling exploiting fluid isomorphisms. *Mon. Wea. Rev.,* **132,** 2882–2894, doi:10.1175/MWR2835.1.

——, D. Ferreira, J. Campin, and D. Enderton, 2007: Mean climate and variability of the atmosphere and ocean on an aquaplanet. *J. Atmos. Sci.,* **64,** 4270–4286, doi:10.1175/2007JAS2226.1.

——, K. C. Armour, J. R. Scott, Y. Kostov, U. Hausmann, D. Ferreira, T. G. Shepherd, and C. M. Bitz, 2014: The ocean's role in polar climate change: Asymmetric Arctic and Antarctic responses to greenhouse gas and ozone forcing. *Philos. Trans. Roy. Soc. London,* **A372,** 20130040, doi:10.1098/rsta.2013.0040.

Molteni, F., 2003: Atmospheric simulations using a GCM with simplified physical parametrizations. I: Model climatology and variability in multi-decadal experiments. *Climate Dyn.,* **20,** 175–191, doi:10.1007/s00382-002-0268-2.

Morrison, A. K., and A. M. Hogg, 2013: On the relationship between Southern Ocean overturning and ACC transport. *J. Phys. Oceanogr.,* **43,** 140–148, doi:10.1175/JPO-D-12-057.1.

Parkinson, C. L., and D. J. Cavalieri, 2012: Antarctic sea ice variability and trends, 1979–2010. *The Cryosphere,* **6,** 871–880, doi:10.5194/tc-6-871-2012.

Polvani, L. M., D. W. Waugh, G. J. P. Correa, and S.-W. Son, 2011: Stratospheric ozone depletion: The main driver of twentieth-century atmospheric circulation changes in the Southern Hemisphere. *J. Climate,* **24,** 795–812, doi:10.1175/2010JCLI3772.1.

Previdi, M., and L. M. Polvani, 2014: Climate system response to stratospheric ozone depletion and recovery. *Quart. J. Roy. Meteor. Soc.,* **140,** 2401–2419, doi:10.1002/qj.2330.

Redi, M. H., 1982: Oceanic isopycnal mixing by coordinate rotation. *J. Phys. Oceanogr.,* **12,** 1154–1158, doi:10.1175/1520-0485(1982)012<1154:OIMBCR>2.0.CO;2.

Sallée, J. B., K. G. Speer, and S. R. Rintoul, 2010: Zonally asymmetric response of the southern ocean mixed-layer depth to the southern annular mode. *Nat. Geosci.,* **3,** 273–279, doi:10.1038/ngeo812.

Sen Gupta, A., and M. H. England, 2006: Coupled ocean–atmosphere–ice response to variations in the southern annular mode. *J. Climate,* **19,** 4457–4486, doi:10.1175/JCLI3843.1.

Sigmond, M., and J. C. Fyfe, 2010: Has the ozone hole contributed to increased Antarctic sea ice extent? *Geophys. Res. Lett.,* **37,** L18502, doi:10.1029/2010GL044301.

——, and ——, 2014: The Antarctic sea ice response to the ozone hole in climate models. *J. Climate,* **27,** 1336–1342, doi:10.1175/JCLI-D-13-00590.1.

——, ——, and J. F. Scinocca, 2010: Does the ocean impact the atmospheric response to stratospheric ozone depletion? *Geophys. Res. Lett.,* **37,** L12706, doi:10.1029/2010GL043773.

Simpkins, G. R., L. M. Ciasto, D. W. J. Thompson, and M. H. England, 2012: Seasonal relationships between large-scale climate variability and Antarctic sea ice concentration. *J. Climate,* **25,** 5451–5469, doi:10.1175/JCLI-D-11-00367.1.

Smith, K. L., L. M. Polvani, and D. R. Marsh, 2012: Mitigation of 21st century Antarctic sea ice loss by stratospheric ozone recovery. *Geophys. Res. Lett.,* **39,** L20701, doi:10.1029/2012GL053325.

Solomon, S., R. W. Portmann, and D. W. J. Thompson, 2007: Contrast between Antarctic and Arctic ozone depletion. *Proc. Natl. Acad. Sci. USA,* **104,** 445–449, doi:10.1073/pnas.0604895104.

Son, S.-W., and Coauthors, 2010: Impact of stratospheric ozone on Southern Hemisphere circulation change: A multimodel assessment. *J. Geophys. Res.,* **115,** D00M07, doi:10.1029/2010JD014271.

Thompson, D. W. J., and S. Solomon, 2002: Interpretation of recent southern hemisphere climate change. *Science,* **296,** 895–899, doi:10.1126/science.1069270.

——, ——, P. J. Kushner, M. H. England, K. M. Grise, and D. J. Karoly, 2011: Signatures of the Antarctic ozone hole in

Southern Hemisphere surface climate change. *Nat. Geosci.,* **4,** 741–749, doi:10.1038/ngeo1296.

Turner, J., and Coauthors, 2009: Non-annular atmospheric circulation change induced by stratospheric ozone depletion and its role in the recent increase of Antarctic sea ice extent. *Geophys. Res. Lett.,* **36,** L08502, doi:10.1029/2009GL037524.

Watterson, I. G., 2000: Southern midlatitude zonal wind vacillation and its interaction with the ocean in GCM simulations.

J. Climate, **13,** 562–578, doi:10.1175/1520-0442(2000)013<0562: SMZWVA>2.0.CO;2.

Winton, M., 2000: A reformulated three-layer sea ice model. *J. Atmos. Oceanic Technol.,* **17,** 525–531, doi:10.1175/ 1520-0426(2000)017<0525:ARTLSI>2.0.CO;2.

Zwally, H. J., J. C. Comiso, C. L. Parkinson, D. J. Cavalieri, and P. Gloersen, 2002: Variability of Antarctic sea ice 1979–1998. *J. Geophys. Res.,* **107,** 3041, doi:10.1029/2000JC000733.